Extragalactic background light inferred from AEGIS galaxy-SED-type fractions

A. Domínguez,[1,2]*† J. R. Primack,[3] D. J. Rosario,[4] F. Prada,[2]‡ R. C. Gilmore,[3,5]
S. M. Faber,[4] D. C. Koo,[4] R. S. Somerville,[6] M. A. Pérez-Torres,[2]
P. Pérez-González,[7]§ J.-S. Huang,[8] M. Davis,[9] P. Guhathakurta,[4] P. Barmby,[10]
C. J. Conselice[11], M. Lozano[1], J. A. Newman[12] and M. C. Cooper[13]

[1]*Departamento de Física Atómica, Molecular y Nuclear, Universidad de Sevilla, Apdo. Correos 1065, E-41080 Sevilla, Spain*
[2]*Instituto de Astrofísica de Andalucía, CSIC, Apdo. Correos 3004, E-18080 Granada, Spain*
[3]*Department of Physics, University of California, Santa Cruz, CA 95064, USA*
[4]*UCO/Lick Observatory, Department of Astronomy & Astrophysics, University of California, Santa Cruz, CA 95064, USA*
[5]*Scuola Internazionale Superiore di Studi Avanzati (SISSA), Via Bonomea 265, 34136 Trieste, Italy*
[6]*Space Telescope Science Institute, 3700 San Martin Drive, Baltimore, MD 21218, USA*
[7]*Departamento de Astrofísica, Facultad de CC. Físicas, Universidad Complutense de Madrid, E-28040 Madrid, Spain*
[8]*Harvard-Smithsonian Center for Astrophysics, 60 Garden Street, Cambridge, MA 02138, USA*
[9]*Department of Astronomy, University of California, Berkeley, CA 94720, USA*
[10]*Department of Physics & Astronomy, University of Western Ontario, London, ON N6A 3K7, Canada*
[11]*University of Nottingham, School of Physics & Astronomy, Nottingham NG7 2RD*
[12]*Department of Physics and Astronomy, University of Pittsburgh, 3941 O'Hara Street, Pittsburgh, PA 15260, USA*
[13]*Steward Observatory, University of Arizona, 933 N. Cherry Avenue, Tucson, AZ, USA; Spitzer Fellow*

ABSTRACT

The extragalactic background light (EBL) is of fundamental importance both for understanding the entire process of galaxy evolution and for γ-ray astronomy, but the overall spectrum of the EBL between 0.1 and 1000 µm has never been determined directly from galaxy spectral energy distribution (SED) observations over a wide redshift range. The evolving, overall spectrum of the EBL is derived here utilizing a novel method based on observations only. This is achieved from the observed evolution of the rest-frame K-band galaxy luminosity function up to redshift 4, combined with a determination of galaxy-SED-type fractions. These are based on fitting Spitzer Wide-Area Infrared Extragalactic Survey (SWIRE) templates to a multiwavelength sample of about 6000 galaxies in the redshift range from 0.2 to 1 from the All-wavelength Extended Groth Strip International Survey (AEGIS). The changing fractions of quiescent galaxies, star-forming galaxies, starburst galaxies and active galactic nucleus (AGN) galaxies in that redshift range are estimated, and two alternative extrapolations of SED types to higher redshifts are considered. This allows calculation of the evolution of the luminosity densities from the ultraviolet (UV) to the infrared (IR), the evolving star formation rate density of the Universe, the evolving contribution to the bolometric EBL from the different galaxy populations including AGN galaxies and the buildup of the EBL. Our EBL calculations are compared with those from a semi-analytic model, another observationally based model and observational data. The EBL uncertainties in our modelling based directly on the data are quantified, and their consequences for attenuation of very-high-energy γ-rays due to pair production on the EBL are discussed. It is concluded that the EBL is well constrained from the UV to the mid-IR, but independent efforts from IR and γ-ray astronomy are needed in order to reduce the uncertainties in the far-IR.

*E-mail: alberto@iaa.es
†Visiting Student at the Santa Cruz Institute for Particle Physics (SCIPP), University of California, Santa Cruz, CA 95064, USA.
‡Visiting Researcher at the Santa Cruz Institute for Particle Physics (SCIPP), University of California, Santa Cruz, CA 95064, USA.
§Associate Astronomer at Steward Observatory, The University of Arizona, Tucson, AZ 85721-0065, USA.

1 INTRODUCTION

The formation and evolution of galaxies in the universe are accompanied unavoidably by the emission of radiation. All this radiated energy is still streaming through the universe, although much is now at longer wavelengths due to redshifting and absorption/re-emission by dust. The photons mostly lie in the range of $\sim$0.1–1000 µm, i.e. ultraviolet (UV), optical and infrared (IR), and produce the second-most energetic diffuse background after the cosmic microwave background, thus being essential for understanding the full energy balance of the universe. We will account in this work for the radiation accumulated by star formation processes through most of the life of the universe, plus a contribution from active galactic nuclei (AGNs) to this wavelength range, known as the diffuse extragalactic background light (EBL).

The direct measurement of the EBL is a very difficult task subject to high uncertainties. This is mainly due to the contribution of zodiacal light, some orders of magnitude larger than the EBL (e.g. Hauser & Dwek 2001; Chary & Pope 2010). There are some measurements in the optical (Bernstein 2007) and in the near-IR (e.g. Cambrésy et al. 2001; Matsumoto et al. 2005), but there is no general agreement about the reliability of these data sets (Mattila 2006). In addition, these near-IR data appear to give intensity levels for the EBL in contradiction to the observation of very-high-energy (VHE; 30 GeV–30 TeV) photons from extragalactic sources (Aharonian et al. 2006; Mazin & Raue 2007; Albert et al. 2008). Little is known about the mid-IR from direct detection due to the higher contamination from zodiacal light at those wavelengths. Measurements with the Far-Infrared Absolute Spectrometer (FIRAS) instrument on board the Cosmic Background Explorer, in the far-IR (Hauser et al. 1998; Lagache et al. 2000) are thought to be more reliable. Other observational approaches set reliable lower limits on the EBL, such as measuring the integrated light from discrete extragalactic sources (e.g. Madau & Pozzetti 2000; Fazio et al. 2004).

There are also other authors who focus on studying galaxy properties based on EBL results (Fardal et al. 2007) or on modelling a region of the EBL spectrum (Younger & Hopkins 2010). On the other hand, there are phenomenological approaches in the literature that predict an overall EBL model (i.e. between 0.1 and 1000 µm and for any redshift). These are basically of the following four kinds.

(i) Forward evolution, which begins with cosmological initial conditions and follows a forward evolution with time by means of semi-analytical models (SAMs) of galaxy formation (e.g. Primack et al. 1999; Somerville et al., in preparation, hereafter SGPD10; Gilmore et al., in preparation, hereafter GSPD10).

(ii) Backward evolution, which begins with existing galaxy populations and extrapolates them backwards in time (e.g. Malkan & Stecker 1998; Stecker, Malkan & Scully 2006; Franceschini, Rodighiero & Vaccari 2008, hereafter FRV08).

(iii) Evolution of the galaxy populations that is inferred over a range of redshifts. The galaxy evolution is inferred here using some quantity derived from observations such as the star formation rate (SFR) density of the universe (e.g. Kneiske, Mannheim & Hartmann 2002; Finke, Razzaque & Dermer 2010; Kneiske & Dole 2010).

(iv) Evolution of the galaxy populations that is directly observed over the range of redshifts that contribute significantly to the EBL. This paper, which we term empirical, belongs to this category.

The type (i) SGPD10 and GSPD10 models discuss the same galaxy formation SAM but in different contexts: SGPD10 contains details of the model used in calculating the bolometric luminosity history of the universe and comparison with data and GSPD10 focuses on the derived EBL and γ-ray attenuation. The SGPD10–GSPD10 model is based on an updated version of the semi-analytic theoretical approach described in Somerville et al. (2008) from the growth of super-massive black holes and their host galaxies within the context of the hierarchical Lambda Cold Dark Matter (ΛCDM) cosmological framework. This is based in part on Somerville & Primack (1999), Somerville, Primack & Faber (2001) and on the simulations summarized by Hopkins et al. (2008a,b). We consider that these types of models are complementary to the observational approach taken here.

We consider the type (ii) FRV08 model the most complete observationally based work of those mentioned above. They base their EBL modelling on galaxy luminosity functions (LFs), quantities which are directly observed and well understood. FRV08 exploit a variety of data to build evolutionary schemes according to galaxy morphology. They account for the contribution from early, late-type galaxies and a starburst population to the EBL. They use observed near-IR LFs from the local universe to $z = 1.4$ for describing the early and late-type galaxies. For the starburst population, they use an optical and only local LF. Different prescriptions are used to extrapolate the evolution of the different morphological types to higher redshifts, and corrections to fit their results to other observational data are applied.

Type (iii) models are not directly based on galaxy data. Instead, they are built from some parametrization of the history of the SFR density. This is a quantity derived using several different methods, each of which has different and significant uncertainties and biases. The SFR density is combined with uncertain assumptions about the emitted galaxy spectral energy distribution (SED) evolution as well.

Our type (iv) EBL estimates (the first approach in this category) will be compared in detail with the type (i) forward evolution semi-analytical galaxy formation model by SGPD10 and GSPD10 and the type (ii) observationally motivated model by FRV08. The other works mentioned are briefly compared with our EBL calculations in Section 6.

Our aim in this paper is to develop an EBL model that is as observationally based and realistic as possible, yet fully reproducible, including a quantitative study of the main uncertainties in the modelling that are directly due to the data. This constrains the range of the background intensity and its implications for γ-ray astronomy. One important application of the EBL for γ-ray astronomy is to recover the unattenuated spectra of extragalactic sources. Our goal is to measure the EBL with enough precision that the uncertainties due to the EBL modelling, in these recovered unattenuated spectra, are small compared with other effects such as systematic uncertainties in the γ-ray observations. Examples of this are discussed in Section 5.

Our model is based on the rest-frame K-band galaxy LF by Cirasuolo et al. (2010, hereafter C10) and on multiwavelength galaxy data from the All-wavelength Extended Groth Strip International Survey (AEGIS;[1] Davis et al. 2007; Newman et al., in preparation) of about 6000 galaxies in the redshift range of 0.2–1.

---

[1] http://aegis.ucolick.org/

These data sets are put together in a very transparent and consistent framework. The C10 LF is used to count galaxies (and therefore to normalize the total EBL intensity) at each redshift. The LF as well as our galaxy sample is divided into three magnitude bins according to the absolute rest-frame *K*-band magnitude, i.e. faint, middle and bright (defined quantitatively later). Within every magnitude bin, an SED type is statistically attached to each galaxy in the LF assuming SED-type fractions that are a function of redshift within those magnitude bins. This is estimated by fitting our AEGIS galaxy sample to the 25 galaxy-SED templates from the SWIRE library. Then, luminosity densities are calculated from these magnitude bins from every galaxy population at all wavelengths, and finally all the light at all redshifts is added up to get the overall EBL spectrum. The results are linked with γ-ray astronomy and with the current understanding of galaxy evolution.

This paper is organized as follows. Section 2 describes the LF, our multiwavelength galaxy catalogue and the galaxy templates. Section 3 explains our methodology. The results for galaxy SED-type fractions, luminosity densities, SFR densities, EBL buildup and EBL intensities are given in Section 4. Section 5 shows the attenuation computed from our EBL model for some VHE sources taken from the literature. In Section 6 our results are discussed including a detailed study of the uncertainties from the modelling and a comparison between our observationally based EBL and that given by theoretical SAMs of galaxy formation. Finally, in Section 7, a summary of our main results and conclusions is presented.

Throughout this paper, a standard ΛCDM cosmology is assumed, with matter density $\Omega_m = 0.3$, vacuum energy density $\Omega_\Lambda = 0.7$ and Hubble constant $H_0 = 70$ km s^{-1} Mpc^{-1}.

2 DATA DESCRIPTION

2.1 *K*-band galaxy luminosity function

The evolving galaxy LF in the rest-frame *K* band provided by C10 from $z = 0$ to 4 is used. This evolving LF is the most accurate measurement to date of cosmological galaxy evolution in the near-IR, where dust absorption is less severe than in optical bands. The *k*-corrections in this band are less severe than in the optical as well. The choice of the C10 LF to normalize the model is also based on the smooth and well-studied shape of the galaxy SEDs in the near-IR, unlike others in UV or mid-IR wavelengths.

The resulting evolving LF is based on the UKIDSS Ultra Deep Survey (Lawrence et al. 2007), which has a large area and depth, and hence reduces the uncertainties due to cosmic variance and survey incompleteness. We refer the reader interested in details to that work. It is important to note that they give a parametrization of the evolution of the LF corrected from incompleteness and fitted by a Schechter function (Schechter 1976) over redshift, $\Phi(M_K^z, z)$, where M_K^z is the rest-frame *K*-band absolute magnitude at redshift *z*. The strongest assumption that they make is to keep constant the faint-end slope α in their parametrization.

2.2 Galaxy sample description

A multiwavelength galaxy catalogue built from AEGIS (Davis et al. 2007; Newman et al., in preparation) for this work is used. This catalogue contains 5986 galaxies, all in the Extended Groth Strip (EGS). It is required that every galaxy in the sample have 5σ detections in the B, R, I, K_S and Infrared Array Camera (IRAC) 1 bands, and observations (but not necessarily detections) in the IRAC 2, 3, 4 and Multiband Imaging Photometer for *Spitzer* (MIPS) 24 bands (see

Table 1. The photometric bands in our galaxy sample. For each we show the effective wavelength, the data source, the requirement for that band to be included for a given galaxy in our sample (det: a detection in this band is required; obs: observation in this band is required, but not necessarily a detection; ext: this band is considered extra information when available) and the 5σ upper limit in that band in cases where there is no detection.

Band	λ_{eff} (μm)	Observatory	Req.	UL (μJy)
FUV	0.1539	*GALEX*	ext	–
NUV	0.2316	*GALEX*	ext	–
B	0.4389	CFHT12K	det	–
R	0.6601	CFHT12K	det	–
I	0.8133	CFHT12K	det	–
K_S	2.14	WIRC	det	–
IRAC 1	3.6	IRAC	det	–
IRAC 2	4.5	IRAC	obs	1.2
IRAC 3	5.8	IRAC	obs	6.3
IRAC 4	8.0	IRAC	obs	6.9
MIPS 24	23.7	MIPS	obs	30

Table 1). These 5σ upper limits are given by the following fluxes: 1.2, 6.3, 6.9 and 30 μJy for IRAC 2, 3, 4 and MIPS 24, respectively, according to Barmby et al. (2008) for the IRAC bands and Dickinson et al. (2007) for MIPS 24. They are also summarized in Table 1. In addition, 1129 of these galaxies have *Galaxy Evolution Explorer* (*GALEX*) detections in the far-UV and 2345 galaxies in the near-UV. In our sample, 4376 galaxies have the highest quality spectroscopic redshifts measured by the Deep Evolutionary Exploratory Probe 2 team (DEEP2 DR3; Newman et al., in preparation), with the Deep Imaging Multi-Object Spectrograph (DEIMOS) spectrograph (Faber et al. 2003) on the Keck II telescope in an area of about 0.7 deg^2 in the sky. All the other galaxies in the sample (1610 galaxies) have secure photometric redshifts, more than 80 per cent with uncertainty in redshift less than 0.1. The redshift covered is between 0.2 and 1 (almost 60 per cent of the age of the universe) for a total sample of 5986 galaxies. For our purpose, we will not distinguish between spectroscopic or photometric redshifts. This assumption will be discussed in Section 6.1.

The optical photometry (*B, R* and *I* bands) was taken from imaging with the CFH12K camera (Cuillandre et al. 2001) on the 3.6-m Canada–France–Hawaii Telescope (CFHT). The integration time for these observations was 1 h in *B* and *R* and 2 h in *I*, per pointing. More details can be found in Coil et al. (2004).

The near-IR photometry in the K_S band is from the Wide-field Infrared Camera (WIRC; Wilson et al. 2003) on the Hale 5-m telescope at the Palomar observatory. This data set is the most restrictive constraint on the area of our sample; therefore, our galaxy catalogue is K_S limited. The EGS field was surveyed to different depths for different sub-regions up to $K_S = 22.5$ in the AB magnitude system. The details can be found in Conselice et al. (2008).

The mid-IR data are from the IRAC and MIPS cameras on board the *Spitzer Space Telescope*. The details can be found in Barmby et al. (2008) and Dickinson et al. (2007) describing the Far Infrared Deep Extragalectic Legacy (FIDEL) survey, the source of our 24-μm data.

In addition, some data in the UV in two different bands of 0.1530 and 0.2310 μm from *GALEX* (Morrissey et al. 2007) are included in our catalogue. This data set is part of the *GALEX* Deep Imaging Survey, and the details can be found in Salim et al. (2009).

A source catalogue from each of these imaging data sets was cross-matched using the Bayesian method, which took into account prior information from the surface densities of sources in each band
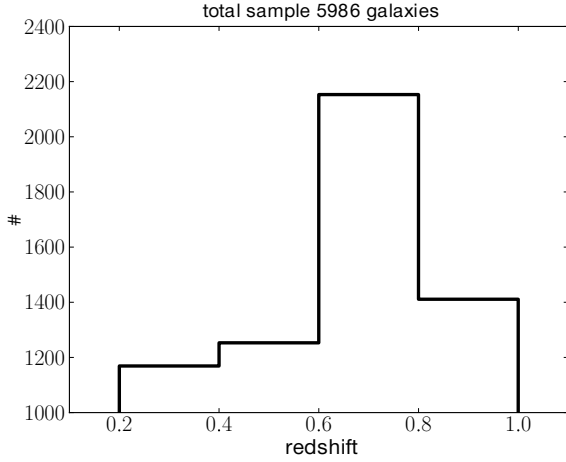
Figure 1. Histogram of the number of galaxies versus redshift of our sample in the four redshift bins considered in this work.

(Huang et al., in preparation). The IRAC 1 data were used as the primary reference catalogue.

It is important to note that all our data are public, except the MIPS 24 photometry, the cross-match catalogue and the photometric-redshift catalogue (Huang et al., in preparation). These will be released to the public soon.

The histogram of the redshift distribution of the AEGIS sample is shown in Fig. 1 in the four redshift bins considered in our calculations. Note the larger number around $z \sim 0.7$, mainly due to the weighting scheme of the DEEP2 survey, which tends to select galaxies at $z > 0.7$ based on colour–colour criteria, plus the effect in the opposite direction of losing faint galaxies at higher redshifts.

In order to calculate the absolute magnitudes in U, B and K bands, we have computed the best-fitting template taken from the Bruzual & Charlot (2003) stellar population models to the data in the photometric bands B, R, I, K_S, IRAC 1 and *FUV*, *NUV* and IRAC 2 when available, using the code Fitting and Assessment of Synthetic Templates (FAST, see the appendix in Kriek et al. 2009 for details). FAST makes a χ^2 minimization from a grid of Bruzual & Charlot (2003) models. We chose a stellar initial mass function (IMF) given by Chabrier (2003), an exponentially declining SFR $\sim \exp(-t/\tau)$ with τ ranging from 10^7 to 10^{10} Gyr (the same range for the ages), metallicities by mass fraction in the range of 0.004–0.050 (solar metallicity is 0.02 in these units) and optical extinction A_v from 0 to 10 following the Calzetti et al. (2000) extinction law. We calculate the absolute magnitudes from the best-fitting model using the U Bessel filter, the B filter from CFHT12K and the same K-band filter from the UKIDSS survey, the same filter where the LF from C10 was estimated. All the transmission curves for these filters can be found in the default distribution of LE PHARE.

The sample was not corrected for incompleteness. However, it is estimated here how this affects our results. The colour-dependent incompleteness of the DEEP2 survey was studied in Willmer et al. (2006). They estimated a relation between the rest-frame $U - B$ colour and the absolute magnitude in the B band M_B for which galaxies fainter than this relation have colour-dependent incompleteness. We show in Fig. 2 colour–magnitude diagrams of our AEGIS galaxy sample for four different redshift bins. The black line is taken from fig. 4 in Willmer et al. (2006). Galaxies located to the right of this line are likely missing. This figure is colour coded according to the calculated best-fitted SWIRE template (see Sections 2.3 and 4.1). The number of galaxies lying to the right of the relation, thus suffering colour-dependent incompleteness, is only of
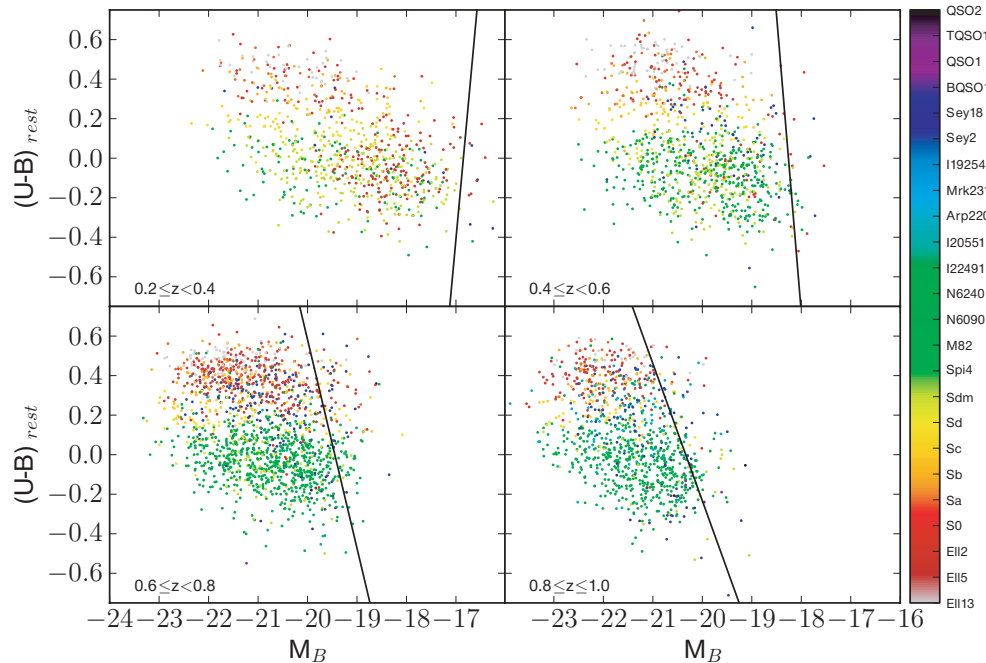
Figure 2. Rest $U - B$ colour versus B-band absolute magnitude diagram for four different redshift bins to illustrate the incompleteness of our galaxy sample after the cuts explained in Section 4.1. The black line is taken from fig. 4 in Willmer et al. (2006). Galaxies to the right of this line may suffer from a colour-selection effect. The fractions of these galaxies are 1.8, 2.3, 7.3 and 9.3 per cent for each of the redshift bins, respectively. The colour code corresponds to the best-fitting galaxy-SED type from the SWIRE library (e.g. Ell13, elliptical 13-Gyr old; Sa, early type spiral; Spi4, very late-type spiral; I20551, starburst; Sey18, Seyfert galaxy 1.8, QSO2, quasi-stellar object with some ratio of optical to IR fluxes). Magnitudes are in Vega system converted from AB system using the relations $U_{\rm Vega} = U_{\rm AB} - 0.73$ and $B_{\rm Vega} = B_{\rm AB} + 0.11$ from Willmer et al. (2006).
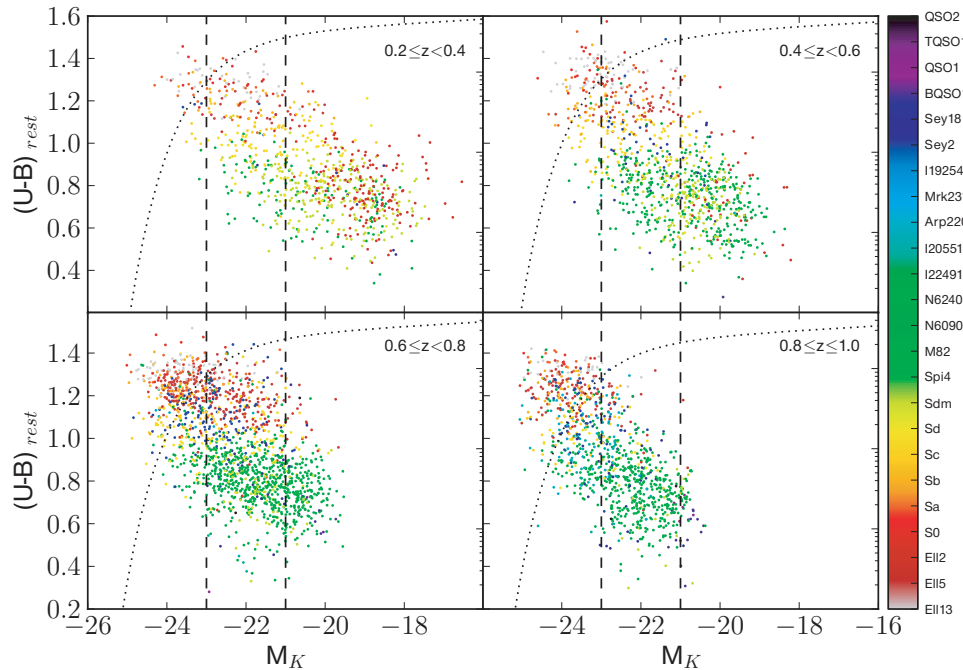
Figure 3. Colour–magnitude diagram in the same four different redshift bins showing the galaxies of our sample after the cuts explained in Section 4.1, for the magnitude bins defined in the text for the integrals in equation (3). The LF by C10 in the mean of every redshift bin with arbitrary units in the logarithmic *y*-axis is overplotted. The colour code is the same as that in Fig. 2. Magnitudes are in the AB magnitude system.

1.8, 2.3, 7.3 and 9.3 per cent for the different redshift bins presented in Fig. 2.

Fig. 3 shows the rest-frame $U - B$ versus absolute magnitude in the K band in the three magnitude bins considered in this work to show an estimation of the galaxy number in each bin and its SED types. We will describe this figure in the context of cosmological evolution in Section 6.4.

Thus to recall, the normalizations of the EBL in our model are given by the K-band LF of C10, and our galaxy-SED-type fractions give the relative contribution of every galaxy type to the total luminosity density. The assignment of SED types to the galaxy population at a given redshift is done individually for three ranges in the K-band absolute magnitude, as will be discussed in Section 3. Moreover, most of the contribution to the EBL (between 70 and 90 per cent) comes from around the knee of the LF ($L_\star$ according to the Schechter parametrization), as shown in Fig. 4 for the rest-frame K-band luminosity density (calculated directly from the integration of the C10 LF), and not from the faintest galaxy population where we suffer some small colour-dependent incompleteness. Fig. 4 also shows that the contribution from the bright end increases with redshift decreasing the impact of any colour-dependent effect. As the remaining colour-independent incompleteness does not have any effect on the galaxy-SED-type fractions in our model or the overall normalization (which is set by the K-band LF), we conclude that our results are quite robust and the effect from incompleteness in our sample is minimal.

2.3 Galaxy spectral energy distribution library

The galaxy SEDs found in the SWIRE template library[2] (Polletta et al. 2007) are used. This library contains 25 templates, representative of the local galaxy population, defined as three elliptical

[2] http://www.iasf-milano.inaf.it/~polletta/templates/swire_templates.html

galaxies, seven spiral galaxies, six starbursts, seven AGN galaxies (three Type I AGN and four Type II AGN) and two composite (starburst+AGN) templates all covering the ∼0.1–1000 μm wavelength range. The elliptical (quiescent), spiral (star-forming) and starburst (very star-forming) IR templates were generated with the GRASIL code (Silva et al. 1998) based on observations. The seven spirals range from early to late types (i.e. S0–Sdm). The starburst templates correspond to the SEDs of NGC 6090, 6240, M82, Arp 220, IRAS 22491−1808 and IRAS 20551−4250. In all of the spiral and starburst templates, the spectral region between 5
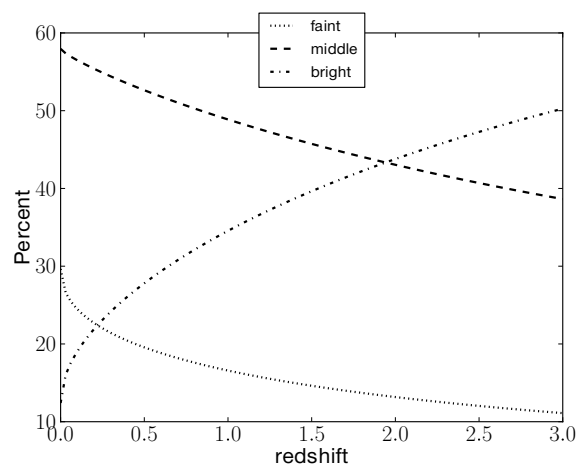
Figure 4. Contribution from the three different magnitude bins defined in Section 3 to the total of the comoving rest-frame K-band luminosity density calculated directly from the LF by C10. The bulk of the light comes from the middle and bright end of the LF, where the Schechter parameter $L_\star$ is. Note the increment with redshift of the bright-end contribution which decreases the impact of a possible colour-selection effect or mis-typing (see Section 6.1) at the highest redshift in our galaxy sample.
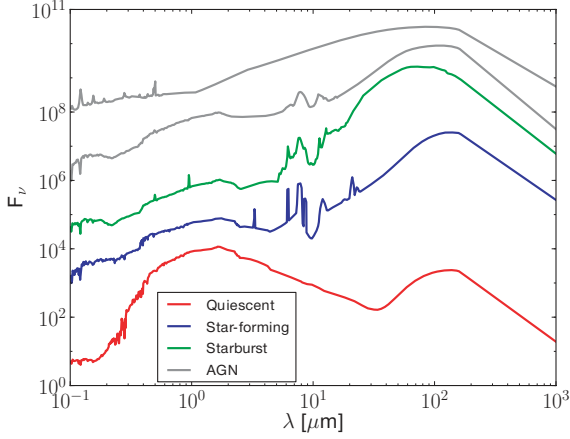
Figure 5. SEDs for some galaxy templates from the SWIRE library. We show here (from the bottom to the top) an early type quiescent galaxy (Ell13), a very late star-forming galaxy (Spi4), a starburst galaxy (I22491) and two different AGN galaxies: a Seyfert II and a quasi-stellar object Type I (QSO1). The *y*-axis is in arbitrary units.

and 12 μm, where many broad emission and absorption features are observed, was replaced by observed IR spectra from the PHT-S spectrometer on board the *Infrared Space Observatory* and from In-frared Spectrometer on *Spitzer*. Some examples of these templates are shown in Fig. 5.

We are aware that these templates do not include high-redshift galaxies ($z > 0.3$). This effect will be taken into account in a future version of our EBL model when higher redshift galaxy SEDs are released, including very vigorous starbursts and AGNs not present in the local universe. The limitation of using local templates for high-redshift galaxies has been addressed in some works such as Murphy et al. (2009), where they conclude that for ultra-luminous IR galaxies (ULIRGs) in the redshift range between $1.4 < z < 2.6$, IR luminosities are overpredicted when they are derived only using MIPS 24 photometry, thus showing a different behaviour than local ULIRGs. It has been also shown by Menéndez-Delmestre et al. (2009) that submillimetre galaxies in the redshift range between $0.65 < z < 3.2$ show a larger polycyclic-aromatic-hydrocarbon (PAH) emission than local analogues, suggesting a more extended dusty star-forming region than seen in local ULIRGS.

3 METHODOLOGY

The empirical approach of the EBL evolution directly observed over the range of redshifts that contribute significantly to the EBL is followed. This is type (iv) according to the classification given in Section 1. As briefly explained in Section 1, our aim is to calculate the EBL integrating over redshift luminosity densities. These quan-tities are estimated attaching statistically SEDs to the galaxies given by the LF by C10 in three different magnitude bins. This is achieved using galaxy-SED-type fractions between $z = 0.2$ and 1 by finding the best-fitting template of the 25 SED templates in the SWIRE library describing every galaxy in the AEGIS galaxy sample. Two different extrapolations for the galaxy-SED-type fractions for $z > 1$ are assumed leading to the same evolving EBL intensity from the UV to the mid-IR but different far-IR.

The LE PHARE v2.2 (Photometric Analysis for Redshift Estima-tions) code is used to find the best-fitting SWIRE SED template for every galaxy in the sample. LE PHARE is a publicly available code[3]

[3] http://www.cfht.hawaii.edu/~arnouts/LEPHARE/cfht_lephare/

(Arnouts et al. 2002; Ilbert et al. 2006) mainly aimed to calculate photometric redshifts, but with the possibility of finding the best-fitting template (among any of the libraries introduced as input) for galaxies with known redshift. LE PHARE makes use of a χ^2 fitting procedure weighted from normalizations in every detected band and with the possibility of setting upper limits for fluxes in some bands based on non-detections. From the fact that we have required observations in several bands to build our catalogue, we set for ev-ery galaxy in the fitting procedure upper limits on the bands where there is no 5σ detection. The information at all bands is used in the fitting.

For every galaxy, templates are rejected if they predict a flux in a given band that is higher than the upper limit for that band. The equations used for the fitting procedure are shown in equation (1), with the parameter *s* given by equation (2):

$$\chi^2 = \sum_i \left(\frac{F_{\text{obs},i} - s\, F_{\text{temp},i}}{\sigma^2} \right)^2 \tag{1}$$

$$s = \sum_j \left(\frac{F_{\text{obs},j} F_{\text{temp},j}}{\sigma_j^2} \right) \Bigg/ \sum_j \left(\frac{F_{\text{temp},j}^2}{\sigma_j^2} \right). \tag{2}$$

The notation is as follows: *i* refers to a given band, *j* to the band used for the scaling, F_{obs} is the observed flux, F_{temp} is the flux from the templates, σ is the 1σ statistical uncertainty of the photometric measurement and *s* is the scaling factor that is chosen to minimize the χ^2 values ($d\chi^2/ds = 0$). For each galaxy in the sample, we use a redshift given by either spectroscopic or photometric data (see Section 2.2 for details of our sample).

We define the comoving luminosity density at the rest-frame wavelength λ as follows:

$$
\begin{aligned}
j_i(\lambda, z) &= j_i^{\text{faint}} + j_i^{\text{mid}} + j_i^{\text{bright}} \\
&= \int_{M_2=-21.0}^{M_1=-16.6} \Phi\left(M_K^z, z\right) f_i\, T_i\left(M_K^z, \lambda\right) (1+z)\, dM_K^z \\
&\quad + \int_{M_3=-23.0}^{M_2=-21.0} \Phi\left(M_K^z, z\right) m_i\, T_i\left(M_K^z, \lambda\right) (1+z)\, dM_K^z \\
&\quad + \int_{M_4=-25.0}^{M_3=-23.0} \Phi\left(M_K^z, z\right) b_i\, T_i\left(M_K^z, \lambda\right) (1+z)\, dM_K^z \\
&\quad\quad (\text{erg s}^{-1}\ \text{Mpc}^{-3}\ \text{Hz}^{-1}),
\end{aligned}
\tag{3}
$$

where M_K^z is the rest-frame absolute magnitude in the *K* band at redshift *z*. The SEDs are given by a function $T_i(M_K^z, \lambda) = L_\nu$ (in units of erg s^{-1} Hz^{-1}) with *i* representing the different SWIRE SED types. We note that this function is dependent on M_K^z, since $T_i(M_K^z, 2.2)$ is the luminosity per Hz at the effective wavelength of 2.2 μm for a galaxy with M_K. The fraction of faint, medium and bright galaxies (f_i, m_i, b_i, the three different magnitude ranges) of each of the 25 classes is taken into account, according to their M_K^z, over redshift.

The magnitude ranges are defined in the rest-frame *K*-band ab-solute magnitude using the AB magnitude system according to the different M_i in the integration limits in equation (3). The faintest magnitude limit corresponds to the faintest galaxy in our sample, the medium range is chosen to lead to roughly equal numbers of galaxies in each bin in the three magnitude bins and the brightest magnitude corresponds to the brightest galaxy in our sample. This separation is done to take into account the fact that for the same fraction of a given SED type, the contribution to the luminosity den-sity will be different depending on luminosity. At any rate, fainter

galaxies than M_1 are too faint to contribute significantly to the EBL even if their number density is fairly large. The same is true for galaxies brighter than M_4: in spite of their high luminosity, their density is not high enough to contribute.

The function $\Phi(M_K^z, z)$ in equation (3) is the Schechter parametrization of the evolving LF as given by C10 in a comoving frame. The factor $(1 + z)$ comes from the k-correction to account for the change in the definition of the local absolute magnitude M_K^0 with the redshift, i.e.

$$k(z) = (1 + z)\frac{T\left(M_K^z, \lambda\right)}{T\left(M_K^0, \lambda\right)}. \tag{4}$$

The comoving total luminosity density is calculated adding the luminosity density from the 25 SWIRE SED types, i.e.

$$j_{\text{total}}(\lambda, z) = \sum_i j_i(\lambda, z). \tag{5}$$

We note that the total luminosity density at 2.2 µm, $j_{\text{total}}(2.2, z)$, is just the integral of the C10 LF.

The quantity defined by equation (5) gives us an estimate of the total amount of light emitted by galaxies per unit volume at a given wavelength and redshift.

The history of the SFR density ρ in the universe is then computed using the following approximation:

$$\rho = 1.74 \times 10^{-10}(j_{\text{IR}} + 3.3 j_{2800})/\text{L}_\odot \quad (\text{M}_\odot \text{ yr}^{-1} \text{ Mpc}^{-3}), \tag{6}$$

where j_{IR} is the total bolometric IR luminosity density integrated from 8–1000 µm, j_{2800} is the luminosity density at 0.28 µm and $\text{L}_\odot = 3.839 \times 10^{33}$ erg s^{-1} is the solar bolometric luminosity. This equation is taken from Wuyts et al. (2009), who add the UV and IR contributions (unobscured plus obscured), using calibrations for the local universe by Kennicutt (1998) and a Salpeter IMF (Salpeter 1955).

If equation (5) is integrated from some redshift z to $z_{\text{max}} = 4$ (up to where the LF is given), then the EBL flux seen by an observer at redshift z, due to the radiation emitted from z_{max} down to z, is obtained:

$$\lambda I_\lambda(\lambda, z) = \frac{c^2}{4\pi\lambda} \int_z^{z_{\text{max}}} j_{\text{total}}[\lambda(1 + z)/(1 + z'), z'] \left|\frac{dt}{dz'}\right| dz'$$
$$(\text{nW m}^{-2} \text{ sr}^{-1}). \tag{7}$$

This is what we call the comoving EBL spectrum, which is given in intensity units. The factor dt/dz' takes into account the assumed cosmology (e.g. Peebles 1993) and is given explicitly by

$$\left|\frac{dt}{dz'}\right| = \frac{1}{H_0(1 + z')\sqrt{\Omega_{\text{m}}(1 + z')^3 + \Omega_\Lambda}} \tag{8}$$

with H_0, Ω_{m} and Ω_Λ being given by the parameters of the ΛCDM cosmology, exactly the same as used by C10 for the LF.

In our approach, it is possible to directly calculate the contribution to the EBL from all redshift bins, as well as the evolution of the EBL spectrum with redshift and the processes related to this evolution, by sources of all the 25 SED types considered.

4 RESULTS

4.1 Galaxy-SED-type fractions

As explained in Section 3, the LE PHARE code is used to fit every galaxy in our sample to the 25 SWIRE templates. For clarity, we will compress in our discussion (but not in our calculations, where they will remain independent) the 25 SED types in the

SWIRE library to four groups: quiescent, star-forming galaxies, starbursts and AGN galaxies. We choose this nomenclature to clarify that our classification is multiwavelength-SED based, and not morphological.

We note that the fitting procedure is relatively sensitive to the errors on the photometric measurements leading to uncertainties in the galaxy-SED-type fractions of ±0.1. For our model, we set a lower limit of 6 per cent to all the photometric errors. The effect of different treatments of errors in the photometry is discussed thoroughly in Section 4 and in this section the uncertainties due to this effect on our galaxy-SED-type fractions and on the EBL estimation are shown.

To avoid accounting for bad fits, which do not correctly describe the galaxy photometric data, a cut in $\chi_{\text{red}}^2 = \chi^2/n$ is applied, with χ^2 given by LE PHARE (equation 1) and n degrees of freedom (bands with detections). We have checked carefully that $\chi_{\text{red}}^2 \leq 30$ is a good value for quiescent, star-forming and starburst galaxies, but AGN galaxies are systematically worse fits, probably due to the fact that there is a large range in AGN SED shapes due to multiple emission components which cannot be easily encapsulated in a few templates.

Fig. 6 shows some examples of good and bad fits for the four different main galaxy types with low χ_{red}^2 in the top row, some fits around $\chi_{\text{red}}^2 \sim 10$ in the second row, other fits around $\chi_{\text{red}}^2 \sim 30$ in the third row and some very bad fits (with very high χ_{red}^2) in the bottom row. Due to the fact that AGN galaxies are systematically worse fits, two different cuts depending on the galaxy-SED type fitted are used for our model. These values are $\chi_{\text{red}}^2 \leq 30$ for quiescent, star-forming and starburst galaxies and $\chi_{\text{red}}^2 \leq 10$ for AGNs. As for the uncertainties on the photometric errors, we show the uncertainties due to these cuts for the galaxy-SED-type fractions and the EBL and discuss them in Section 6.1.

After applying these cuts, 4467 galaxies still remain, i.e. ~75 per cent of the original sample. Fig. 7 shows a histogram of the galaxy-SED types in the total sample after the cuts, and the classification (shown with different colours) of the four main galaxy groups considered in this discussion. We find 19 per cent quiescent, 67 per cent star-forming galaxies, 5 per cent starbursts and 8 per cent AGN galaxies.

A bimodality between quiescent and star-forming galaxies is clearly found. Most of the quiescent galaxies are $\leq$5-Gyr-old, late-type elliptical (Ell5 and Ell2, according to the SWIRE classification). The bulk of the star-forming population is late-type spirals with the PAH region being measured using *Spitzer* data (Spi4, according to the SWIRE classification). In the starburst-like galaxies case, the Arp 220-like galaxies are dominant. The AGN-like population is clearly dominated by Seyfert-type galaxies, especially type 2.

Table 2 and Fig. 8 show the galaxy-SED-type fractions for four different redshift bins up to $z = 1$, where we have chosen bins of $\Delta z = 0.2$ for statistical reasons. The shadow regions are the uncertainties due to the lower limits on the photometric errors for the catalogue and for the χ_{red}^2 cuts. This region is calculated changing the lower limits from 1 to 10 per cent in steps of 1 per cent and applying extreme cases for the cuts for every lower limit. The boundaries from these calculations lead to the shadow regions. The fractions adopted for the model are marked with crosses and wider lines. We observe that the fraction of quiescent galaxies increases by a factor of ~2 from $z \sim 0.9$ to 0. 3, while the star-forming fraction keeps roughly constant for the full redshift range peaking at $z = 0.5$. Starburst-type galaxies decrease very quickly from $z \sim 0.9$ and reach almost 0 at $z \sim 0.5$. On the other hand, the AGN-type fraction
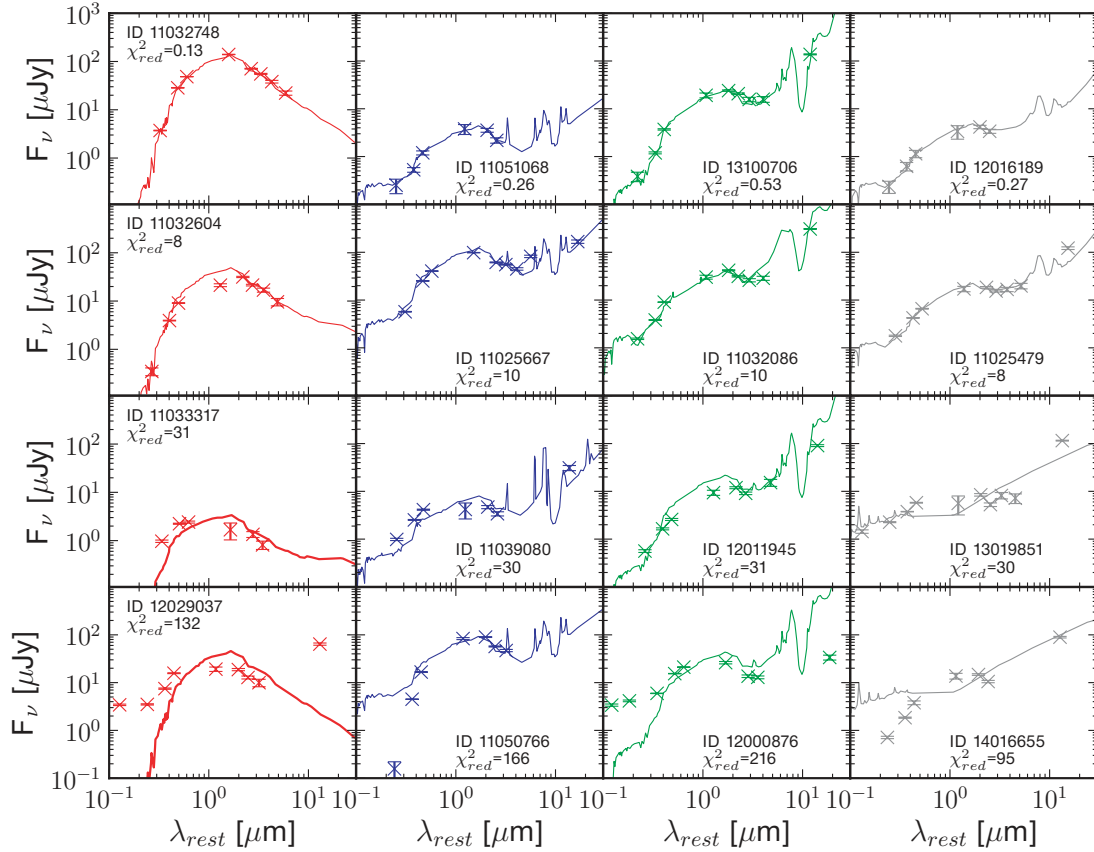
Figure 6. Examples of the best fits (top row), fits around $\chi^2_{red} = 10$ (second row), fits around $\chi^2_{red} = 30$ (third) and the worst fits (bottom row). The columns are from left to right: quiescent, star-forming galaxies, starbursts and AGN galaxies. The AEGIS identification number is shown for the galaxy along with χ^2_{red} given by the fitting code LE PHARE described in Section 3. The information at all bands is used in the fitting.
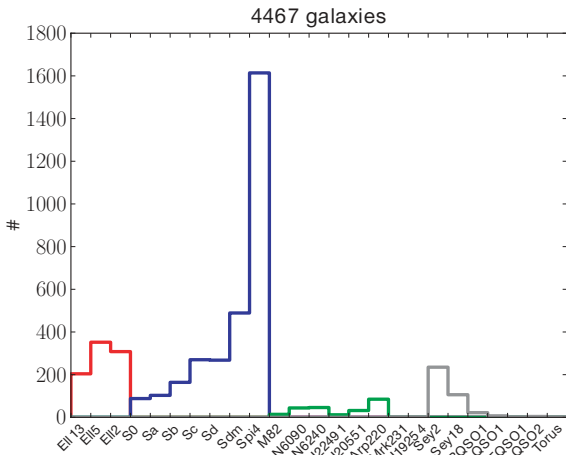
Figure 7. Galaxy-SED types for the sample after removing the worst fits ($\sim$25 per cent of the total sample; see Section 4.1). We have 864 quiescent (in red, 19 per cent), 2996 star-forming galaxies (in blue, 67 per cent), 233 starbursts (in green, 5 per cent) and 374 AGN galaxies (in grey, 8 per cent) from a total of 4467 galaxies. The x-axis describes the names of the 25 SED templates from the SWIRE library.

is roughly constant from $z \sim 0.9$ to 0.7 and then decreases to 0.02 at $z \sim 0.3$. This result should not be considered a complete picture of the evolution of the galaxy populations in the universe since these fractions depend on the colour–magnitude limits of the survey as Fig. 2 shows. But what is certainly described is the population of

galaxies that contribute the most to the EBL around the knee of the LF (the middle and bright region of the LF; see Fig. 4).

Fig. 9 shows the galaxy-SED-type fractions for the three different magnitude bins defined in equation (3) and explained in Section 3. These are the galaxy-SED-type fractions used directly in equation (3) to calculate the luminosity densities. Table 3 lists the number of galaxies in every magnitude and redshift bin used to estimate the galaxy-SED-type fractions shown in Fig. 9.

The galaxy-SED-type fractions are extrapolated to lower redshift ($z \sim 0$) by using results from Goto et al. (2003), who use data from the Sloan Digital Sky Survey (SDSS). They give galaxy fractions according to a morphological classification. They are converted to SED classification by using two different observational works, using the Galaxy Zoo catalogue from SDSS data, on the abundances of blue-elliptical galaxies ($f_{be} = 5.7 \pm 0.4$ per cent; Skibba et al. 2009) and red spirals ($f_{rs} \sim 25$ per cent; Schawinski et al. 2009). Utilizing these works, we calculate galaxy-SED-type fractions for the local $0 < z < 0.2$ universe as follows: in figs 12 and 15 of Goto et al. (2003), we see morphology–density and morphology–radius relations, respectively. From the bin that has the largest number density in either of these figures, we have fractions of galaxies with early ($\sim$14 per cent), intermediate-type ($\sim$26 per cent), early disc ($\sim$35 per cent) and late-disc ($\sim$25 per cent) morphology. The fractions of ellipticals are the fractions of early galaxies, $f_{ell} \sim 14$ per cent, and the fractions of spirals are of the intermediate-type plus the early disc plus late-disc galaxies, $f_{spi} \sim 86$ per cent. From the Galaxy Zoo papers (Schawinski et al. 2009; Skibba et al. 2009), these fractions are estimated for

Table 2. Galaxy-SED-type fractions for our galaxy sample after applying the $\chi^2_{\rm red}$ cuts (see Section 4.1). Numbers are shown for galaxies non-rejected and rejected by the cuts, respectively. The total of non-rejected plus rejected galaxies is 5828. This is less than 5986, our total number of galaxies, because LE PHARE could not get any fit for 158 galaxies.

$z_{\rm mean}$	Quiescent	Star-forming	Starburst	AGN	Total non-rejected/rejected
0.3	235 (29 per cent)/77 (24 per cent)	554 (69 per cent)/169 (52 per cent)	1 (0 per cent)/23 (7 per cent)	14 (2 per cent)/55 (17 per cent)	804/324
0.5	157 (16 per cent)/38 (16 per cent)	756 (77 per cent)/133 (47 per cent)	13 (1 per cent)/13 (5 per cent)	58 (6 per cent)/67 (32 per cent)	984/241
0.7	328 (20 per cent)/59 (13 per cent)	1079 (66 per cent)/149 (32 per cent)	55 (3 per cent)/38 (8 per cent)	175 (11 per cent)/221 (47 per cent)	1637/467
0.9	144 (14 per cent)/22 (7 per cent)	607 (58 per cent)/104 (32 per cent)	164 (16 per cent)/21 (6 per cent)	127 (12 per cent)/182 (55 per cent)	1042/329
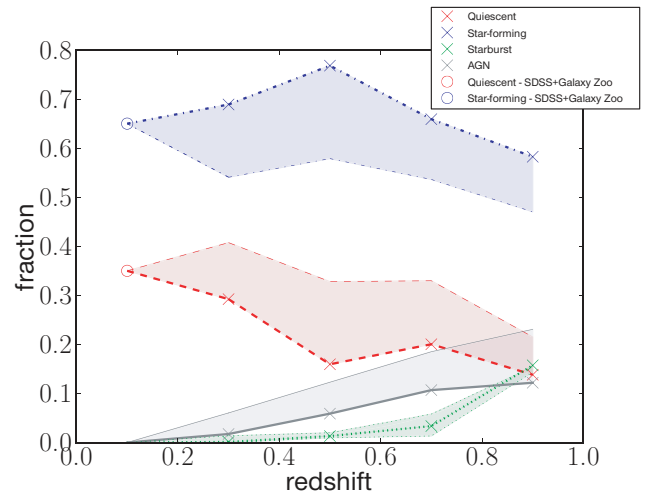
Figure 8. Galaxy-SED-type fractions from our catalogue (after the $\chi^2_{\rm red}$ cuts; see Section 4.1) of the different populations versus redshift according to our multiwavelength fits. We mark with crosses our fractions from $z = 0.9$ to 0.3. The lines represent the linear interpolation that we use to calculate galaxy-SED-type fractions for all redshift: dashed red line represents quiescent galaxies, dot–dashed blue line represents star-forming galaxies, dotted green line represents starburst galaxies and solid grey line represents AGN galaxies. The circles at $z = 0.1$ are fractions computed from the SDSS-based sample (see the text). We show with a shadow area the uncertainties from our lower limit for the errors as well as for our $\chi^2_{\rm red}$ cut for fits. The uncertainties are around ± 0.1.

the local universe according to equations (9) and (10): $f_{\rm quies} \sim 35$ per cent of quiescent and $f_{\rm sf} \sim 65$ per cent of star-forming galaxies:

$$f_{\rm quies} = f_{\rm ell} - (f_{\rm ell} \times f_{\rm be}) + (f_{\rm spi} \times f_{\rm rs})$$
$$= 0.14 - (0.14 \times 0.057) + (0.86 \times 0.25) = 0.35 \qquad (9)$$

$$f_{\rm sf} = f_{\rm spi} - (f_{\rm spi} \times f_{\rm rs}) + (f_{\rm ell} \times f_{\rm be})$$
$$= 0.86 - (0.86 \times 0.25) + (0.14 \times 0.057) = 0.65. \qquad (10)$$

We have to keep in mind that these numbers are calculated from a different sample, and a direct comparison with our sample may not be accurate. Note as well that our definition for quiescent and star-forming is not exactly the same as the red and blue classification from Galaxy Zoo but very similar. Some of our very early type star-forming galaxies are red according to that classification, but the results do not change much because of the fewer number of these galaxies. In the opposite direction to this effect, we note as well that LE PHARE prefers to fit some early type star-forming galaxies as late-type red galaxies due to their bluer optical colours but very little dust re-emission, if any, according to the SWIRE templates.

To be able to compute the local EBL with accuracy, as well as its evolution out to the redshifts of the most distant objects detected by ground-based VHE γ-ray telescopes, i.e. $z \leq 0.6$ (Albert et al. 2008), we would need to extrapolate the galaxy-SED-type fractions to $z > 1$. It is expected that the local EBL has contributions from these larger redshifts, although the behaviour is different for the optical/near-IR and the far-IR due to the spectral region where the different populations contribute.

For the high-redshift universe ($z > 1$, where there are no galaxies in our sample), two different cases are considered for the evolution of the galaxy-SED-type fraction. It is shown that our results are not changed significantly except in the far-IR by these two choices. For the redshifts less than those of the most distant known γ-ray
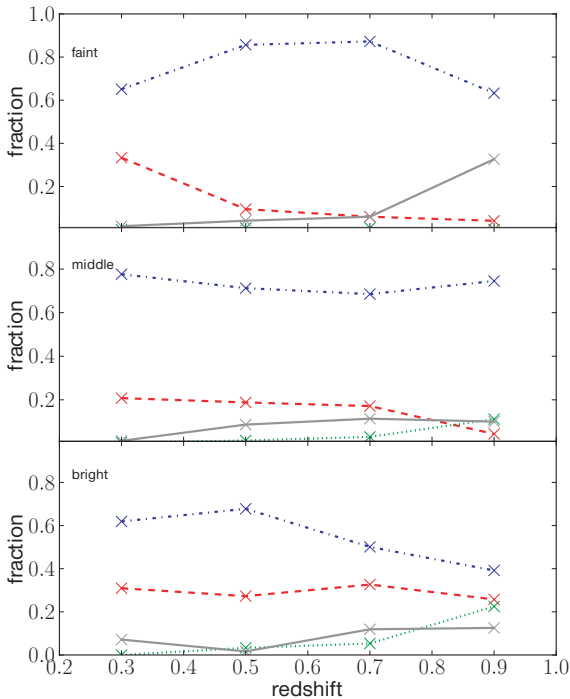
Figure 9. Galaxy-SED-type fractions (after applying the $\chi^2_{\rm red}$ cuts; see Section 4.1) of the different populations (the lines are the same as in Fig. 8) versus redshift in the three different magnitude bins defined in the text for equation (3). See Table 3 for the number of galaxies in every magnitude and redshift bin.

Table 3. Number of galaxies (after applying the $\chi^2_{\rm red}$ cuts; see Section 4.1) in every magnitude and redshift bin used to calculate the galaxy-SED-type fractions in Fig. 9.

	$z = 0.3$	0.5	0.7	0.9	Total
Faint	507	411	251	49	1218
Middle	255	452	899	530	2136
Bright	43	121	487	462	1113

sources, and redshifts where future sources are likely to be found in the near future by Imaging Atmospheric Cherenkov Telescopes (IACTs), we find that there is almost no change in the EBL even with a fairly large adjustment in the evolution of galaxy-SED-type fractions. This is discussed in Section 6.1 and here we show the uncertainties of the EBL and other quantities calculated due to these assumptions. The *fiducial* choice is to keep constant the fractions computed for our highest redshift bin. This choice is made for simplicity, due to the difficulty in the multiwavelength classification of distant galaxies with current instruments. But we do note that there is strong evidence from several observational results by Reddy et al. (2005), Pérez-González et al. (2008), Taylor et al. (2009) and Wuyts et al. (2009) which suggest no further evolution at higher redshifts of the quiescent population. All these independent works claim that the fraction of distant non-star-forming red objects in the high-redshift universe keep constant around 24–33 per cent of the total number of galaxies up to $z > 2.5$. We find at $z \sim 0.9$ around 14 per cent of quiescent galaxies, which are kept constant for higher redshifts. We note here the red-galaxy incompleteness for DEEP2, implying that our fractions might underestimate the actual number of mainly quiescent galaxies in the faint end of the LF (as seen in

the very low number of quiescent fractions in Fig. 9), due to the difficulty of the DEEP2 survey in characterizing faint-red galaxies for $z > 0.8$. The impact of this effect is decreased by taking into our catalogue galaxies with photometric redshift. In any case, there are no consequences for the EBL results as previously discussed in Section 2.2, because the bulk of the light comes from the region of the LF around $L_\star$ where we are basically complete.

As an alternative approach, we choose to increase linearly with redshift the starburst-like fraction from our calculated 16 per cent at $z = 0.9$ up to 60 per cent at $z = 2$, while decreasing at the same rate the quiescent and star-forming galaxies. The weight of each of the 25 SWIRE templates is changed in the same proportion. The fractions are kept constant at $z = 2$ for $z > 2$. This approach is called *high starburst* and it is used to determine a likely upper limit on the EBL at long wavelengths (see Section 4.3).
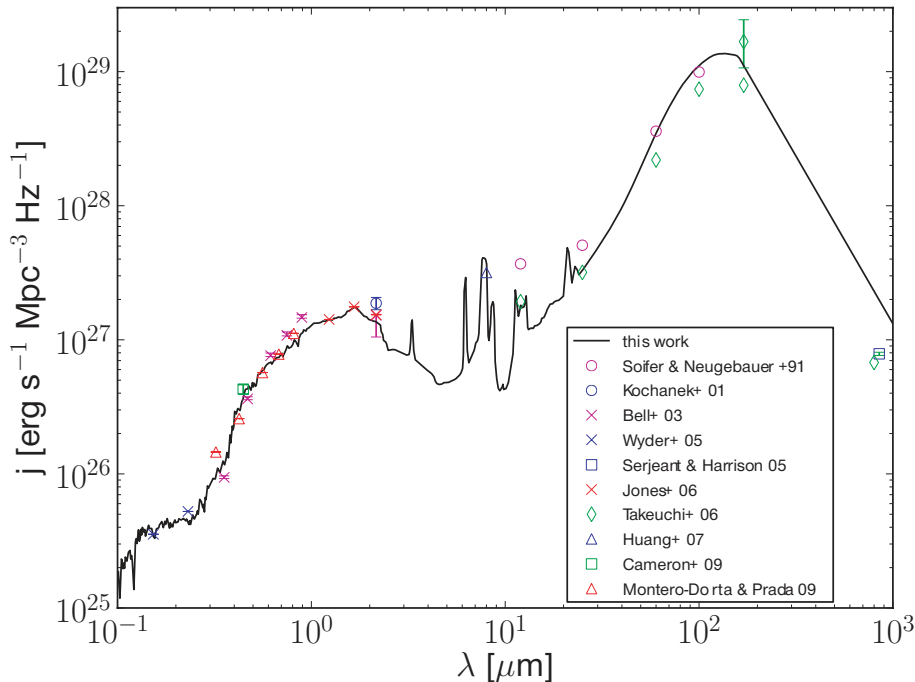
4.2 Luminosity densities

The local galaxy luminosity density is shown in Fig. 10 calculated using equation (5). The solid black line is computed from the sum of the contributions of all the 25 SED types. An excellent agreement is found with the observational data from independent surveys over all wavelengths. We note that our different assumptions for the high-redshift fractions lead necessarily to the same result because this is the light emitted at $z = 0$.

Fig. 11 shows the evolution over redshift of the luminosity densities at different wavelengths for both of our extrapolations for the high-redshift fractions. We show with a dot–dashed orange line the galaxy formation SAM prediction by SGPD10 and defer the discussion to Section 6.3. The upper-left panel shows the rest-frame $0.28\,\mu$m, which is in good agreement with the observational results by Gabasch et al. (2006) and Dahlen et al. (2007) for $z < 1.5$ and somewhat lower between $z = 2$ and 1.5 than the Dahlen et al. (2007) data. This quantity is also directly related to the SFR density through equation (6). The upper-right panel shows the rest-frame B band, which is in good agreement with some observational results, such as those of Norberg et al. (2002), Gabasch et al. (2004) and Ilbert et al. (2005), but around 15–20 per cent higher than the results of Faber et al. (2007). At $z > 1$, we are a factor of ~ 2 higher than the data by Dahlen et al. (2005). The lower-left panel shows the rest-frame K band, among some observational results by Arnouts et al. (2007) and Barro et al. (2009). The lower-right panel shows the evolution of our calculated total IR luminosity over redshift, total IR luminosity given by the FRV08 model and from observations by Rodighiero et al. (2010). We note a general good agreement with these data (we are a factor of 1.5 higher around $z \sim 1$) for our *fiducial* extrapolation of SED types beyond $z = 1$, but predict a higher luminosity density for the *high-starburst* assumption. The agreement with FRV08 is pretty good, except for the lowest redshifts. The total IR luminosity is also directly related to the SFR density through equation (6).

4.3 Star formation rate density history

Fig. 12 shows the history of the SFR density of the universe computed from our modelling using equation (6). It also shows the prediction made by using the same equation from the luminosity densities provided by SGPD10 and from a compilation of observational works of Pérez-González et al. (2008) using different estimators, assuming a Salpeter stellar IMF. We are aware that this IMF is not as good a description of the observations as other IMFs such as Chabrier (2003), but we are concerned here about showing

Figure 10. Comparison between our estimation of the local luminosity density (black line) and observational data from different surveys: 12, 25, 60, 100 μm from Soifer & Neugebauer (1991); *K* band from Kochanek et al. (2001); *u, g, r, i, z, K* band from Bell et al. (2003); *FUV, NUV* from Wyder et al. (2005); 850 μm from Serjeant & Harrison (2005); *bj, rf, J, H, K* bands from Jones et al. (2006); 12, 25, 60, 100, two different analysis for 170, 800 μm from Takeuchi et al. (2006) (two different analysis); 8 μm from Huang et al. (2007); *B* band from Driver et al. (2008) and Cameron et al. (2009); and *u, g, r, i, z* from Montero-Dorta & Prada (2009).

a comparison with the compilation of SFR data, which is given by a Salpeter IMF. The data from $z = 3$–1.5 are roughly reproduced. Our results are in agreement within errors with the upper data envelope from $z = 1.5$–0.7. We systematically predict a factor of $\sim$1.3 higher SFR than the observational data between $z = 0.7$ and 0. For the *high-starburst* assumption, a considerably higher SFR density is estimated. This *high-starburst* case is motivated by the increasing SFR density to $z \sim 2$ in Fig. 12 and the increasing specific SFR to $z \sim 2$ (Reddy et al. 2006; Daddi et al. 2007). But Fig. 12 also indicates that our *high-starburst* is an extreme assumption.

We want to call attention to the large uncertainties on the observational data estimates for the SFR for all redshifts. These uncertainties are especially important for the higher redshifts, mainly because local calibrations are used in the estimations, and also the uncertainties of the corrections due to dust absorption. The same is true for equation (6) which is calibrated using observed local galaxy properties, and these might indeed evolve in redshift.

4.4 Extragalactic background light

The local EBL ($z = 0$) estimated using our method is shown in Fig. 13. The solid black line is the EBL calculated by our *fiducial* model[4] using equation (7). Observational data from direct measurements (empty symbols) and from galaxy counts (filled symbols) are plotted. It is usual to consider data from galaxy counts as lower limits. We find a very low background from UV to mid-IR, along the lower limits from galaxy counts. In the UV our model is lower than the Gardner, Brown & Ferguson (2000) data, but we consider these data suspect, due to very poor statistics on their number counts

---

[4] Intensity files at different redshifts are publicly available at http://side.iaa.es/EBL/

at the faintest magnitudes and due to the fact that they are systematically higher than the UV data from *GALEX* (Xu et al. 2005), an experiment with higher sensitivity and better statistics.

In the mid-IR region between 7 and 15 μm, our results are a factor of $\sim$1.2 higher than other models. A lower background than FRV08 is estimated from 15–50 μm by a factor as large as $\sim$1.5. Our results are still compatible with the limits from galaxy counts. On the contrary, we predict the same far-IR light as FRV08 and a factor of $\sim$2–3 larger than GSPD10, higher than the galaxy counts and in very good agreement with most of the direct measurements. The high flux we predicted in the far-IR (in comparison to GSPD10) is a characteristic of the SWIRE galaxy SEDs we use, given by the GRASIL code which is used to calculate the far-IR emission, and the relation between the near-IR and the far-IR in the templates.

In the same figure, we also plot upper limits using solid coloured lines from γ-ray attenuation studies. The cyan and yellow solid lines by Mazin & Raue (2007) were computed for the so-called *realistic* and *extreme* cases, where the authors considered different upper limits for the spectral slopes of VHE emission from blazars of $E^{-1.5}$ (Aharonian et al. 2006; Albert et al. 2008) and $E^{-2/3}$, respectively. Our calculation is compatible with the upper limits from the extreme case, but marginally disagrees with the realistic case for the largest wavelengths. We will discuss these issues further in Section 5.

Fig. 13 also shows the uncertainties in our modelling due to the uncertainties on the Schechter parameters of the LF given by C10, the errors in the photometric catalogue, as explained at the beginning of this section, the uncertainties on the χ^2_{red} cut applied and uncertainties due to the extrapolations for the galaxy-SED types for $z > 1$. All the possibilities are calculated and the extreme cases are plotted. The uncertainties from the UV up to the mid-IR are dominated by the errors in the photometry and the cuts. The directions from both effects are different: the uncertainties from the
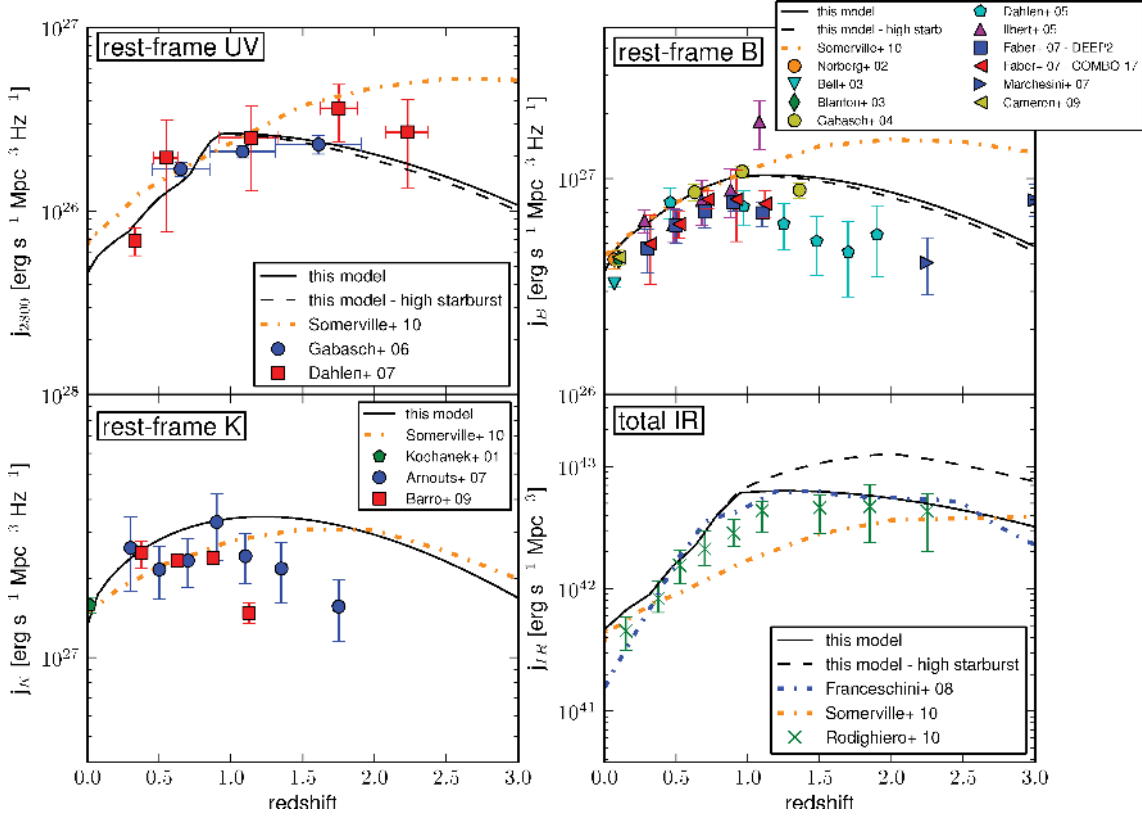
Figure 11. Comparison between the calculated luminosity densities versus redshift for different spectral bands with observational data (solid black line, for our *fiducial* extrapolation; dashed black line for our *high-starburst* extrapolation for the galaxy-SED-type fractions for $z > 1$; see Section 4.1). We also show as a dot–dashed orange line the model from SGPD10. *Upper-left panel*: rest-frame UV at 0.28 μm and data from Gabasch et al. (2006) and Dahlen et al. (2007). *Lower-left panel*: rest-frame K band and observational data from Arnouts et al. (2007) and Barro et al. (2009). It is important to note that this is just the integral of the LF by C10 between M_1 and M_4 in equation (3). *Upper-right panel*: rest-frame B band and observational data from a compilation by Faber et al. (2007) of these works: Norberg et al. (2002), Bell et al. (2003), Blanton et al. (2003a), Gabasch et al. (2004), Dahlen et al. (2005) and Ilbert et al. (2005). Data from Marchesini et al. (2007) and Cameron et al. (2009) are plotted as well. *Lower-right panel*: integrated IR from 8–1000 μm data from Rodighiero et al. (2010) and the phenomenological estimations by FRV08.
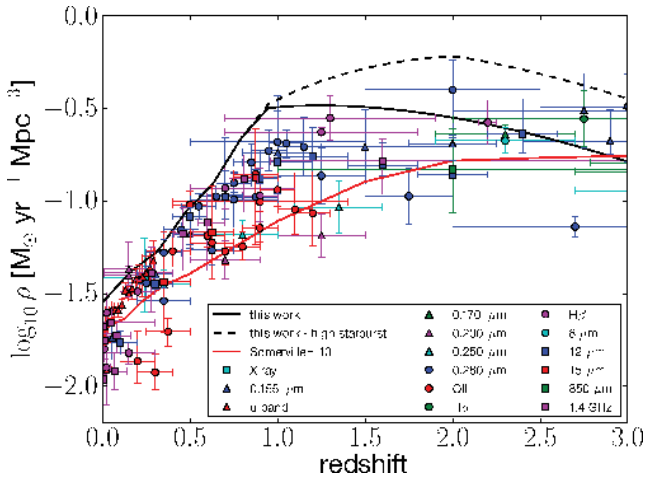

Figure 12. Comparison between the calculated SFR density computed using equation (6) for a Salpeter IMF, the prediction using the same equation from the luminosity densities provided by SGPD10 (solid red line) and some observational data from different estimators shown in the legend. The compilation of data points is taken from Pérez-González et al. (2008). The solid and dashed black lines are from the different extrapolations for the galaxy-SED-type fractions for $z > 1$ (see Section 4.1).

photometry are below the *fiducial* model and the uncertainties from the cuts are above it. In the far-IR, the uncertainties in the extrapolations to $z > 1$ dominate with a factor of ∼1.5. These effects will be thoroughly discussed in Section 6.1.

The evolution of the EBL is important to account for the history of the galaxy emission and the processes involved as well as to properly calculate the attenuation for VHE γ-rays for the high-redshift universe. We show in Fig. 14 the comoving intensity level of the EBL for different redshifts, the contribution to the EBL at those redshifts from the four main SED groups to our *fiducial* extrapolation and the predictions for the EBL by other models. In Table 4 we quantify this evolution, where the bolometric intensity is defined according to equation (11), i.e.

$$I_{bol} = \int \nu I_\nu \, d\ln \nu. \tag{11}$$

We should note that the starburst population contributes 54 per cent to the comoving bolometric EBL at $z = 2$, but only 30 per cent for the local universe. We note as well that the far-IR peak in the SED is higher relative to the near-IR peak at these redshifts; this is due to the fact that a large fraction of the energy radiated from starburst systems is at far-IR wavelengths. We also note that the total bolometric intensity peaks at $z \sim 0.6$–0.2, because the far-IR peaks at higher energetic wavelengths there as shown in Fig. 14.
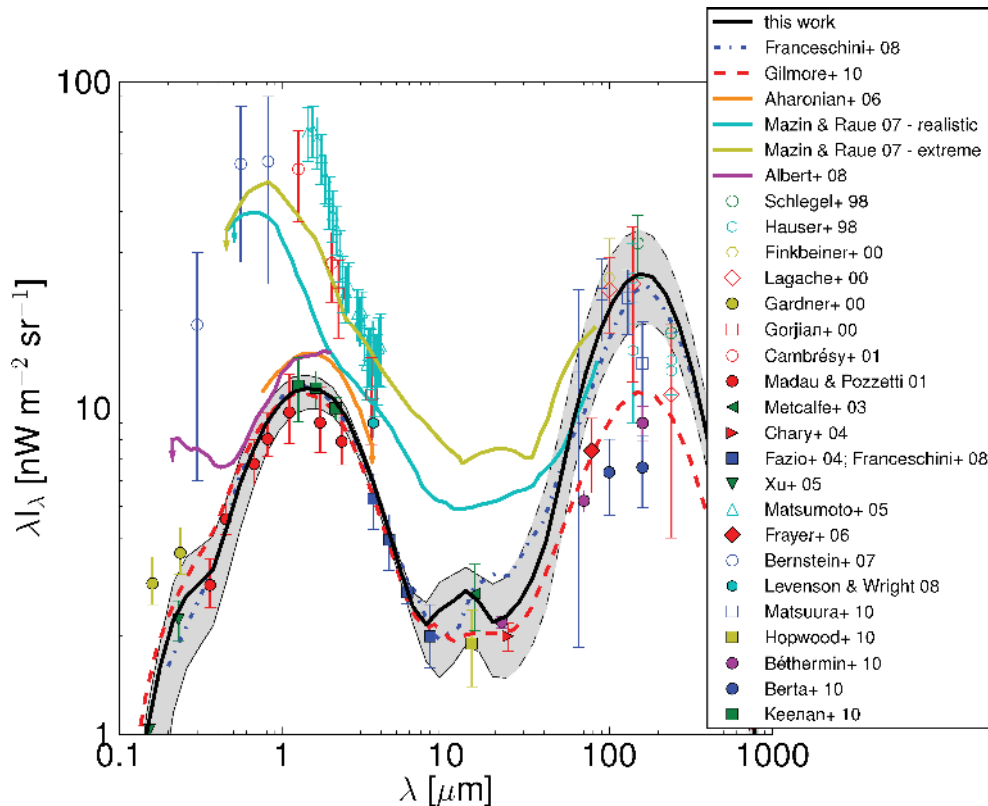
Figure 13. The solid black line is the EBL calculated by the *fiducial* extrapolation of the galaxy-SED-type fractions for $z > 1$. Empty symbols are direct measurements: 0.3, 0.555, 0.814 μm by Bernstein (2007); 1.43, 1.53, 1.63, 1.73, 1.83, 1.93, 2.03, 2.14, 2.24, 2.34, 2.44, 2.54, 2.88, 2.98, 3.07, 3.17, 3.28, 3.38, 3.48, 3.58, 3.68, 3.78, 3.88, 3.98 μm by Matsumoto et al. (2005) using Infrared Telescope in Space (IRTS); 1.25, 2.2 μm (slightly shifted for clarity) by Cambrésy et al. (2001); 2.2, 2.5 μm by Gorjian, Wright & Chary (2000); 60, 100 μm by Finkbeiner, Davis & Schlegel (2000) all these using Diffuse Infrared Background Experiment (DIRBE); 65, 90, 140 (slightly shifted for clarity), 160 μm by Matsuura et al. (2010) using AKARI; 100, 140, 240 μm by Lagache et al. (2000); 140 (slightly shifted for clarity), 240 μm by Schlegel, Finkbeiner & Davis (1998); 140, 240 μm by Hauser et al. (1998) all these using FIRAS. Filled symbols are galaxy-count data, usually considered lower limits: 0.1530, 0.2310 μm by Xu et al. (2005) using *GALEX*; 0.1595, 0.2365 μm by Gardner et al. (2000) using *HST* and Space Telescope Imaging Spectrograph; 0.36, 0.45, 0.67, 0.81, 1.1, 1.6 (slightly shifted for clarity), 2.2 μm (slightly shifted for clarity) by Madau & Pozzetti (2000) using *HST* and ground-based telescopes; 1.25, 1.60, 2.12 μm by Keenan et al. (2010) using Subaru; 3.6 μm by Levenson & Wright (2008); 3.6, 4.5, 5.8, 8.0 μm by Fazio et al. (2004) with a re-analysis of the last point by FRV08, all of these using IRAC; 15 μm by Metcalfe et al. (2003) using *Infrared Space Observatory*; 15 μm by Hopwood et al. (2010) using AKARI; 24 μm by Papovich et al. (2004) and Chary et al. (2004); 24 (slightly shifted for clarity), 70, 160 μm by Béthermin et al. (2010) using MIPS; 71.4 μm by Frayer et al. (2006) using MIPS; 100, 160 μm by Berta et al. (2010) using *Herschel*. The coloured solid lines (Aharonian et al. 2006; Mazin & Raue 2007; Albert et al. 2008) are upper limits from γ-ray astronomy using different blazars (see Section 5 for details). The dot–dashed blue line and the dashed red line are the predictions from the models by FRV08 and GSPD10, respectively. Uncertainties in our EBL estimation are shown with a shadow area. These EBL uncertainties include the uncertainties in Schechter parameters of the LF by C10, photometric errors in the galaxy catalogue, χ^2_{red} cuts applied and extrapolations of the galaxy-SED-type fractions for $z > 1$ (see Section 4.1). The envelope of the shadow region within the dashed line at wavelengths above 24 μm shows the region where there is no photometry in our galaxy catalogue. The EBL uncertainties are thoroughly discussed in Section 6.1.

Another important observable is the buildup of the local intensities for different wavelengths. This is the fraction of the local EBL at a given wavelength that was already in place at a given redshift. This is shown in Fig. 15 for several wavelengths. As an example, we see that ∼70 per cent of the local EBL at $\lambda = 0.445$ and 2.2 μm comes from $z < 1$, 50 per cent of the EBL below ∼180 μm was already in place at $z = 1$, but it is only ∼40 per cent at 240 μm. It is significant that the EBL at shorter wavelengths mostly come from sources at much lower redshifts than the larger ones (see Lagache, Puget & Dole 2005).

Fig. 16 shows a comparison between the EBL buildup for our model, FRV08, GSPD10 and the observational work by LeFloc'h et al. (2009) based on data from MIPS at 24 μm up to $z \sim 1.5$ in the Cosmological Evolution Survey (COSMOS) field. The main contribution to the EBL at 24 μm comes from star-forming and starburst-type galaxies. This region of the SEDs is highly dependent

on the non-smooth PAH features. We observe a general agreement, but reach a factor of 40 per cent difference at $z \sim 1.2$ for the *fiducial* extrapolation. The uncertainties here are large (see Section 6.1).

5 γ-RAY ATTENUATION

5.1 γ-ray attenuation from this EBL model: theoretical background

The EBL has important implications for the interpretation of data taken using recent VHE experiments (the *Fermi* satellite, Gehrels & Michelson 1999; IACTs, such as Major Atmospheric Gamma Imaging Cherenkov (MAGIC), Very Energetic Radiation Imaging Telescope Array Systems (VERITAS) and High Energy Stereoscopic System (HESS); Lorenz 2004; Weekes et al. 2002; Hinton 2004, respectively), due to the photon–photon pair production between
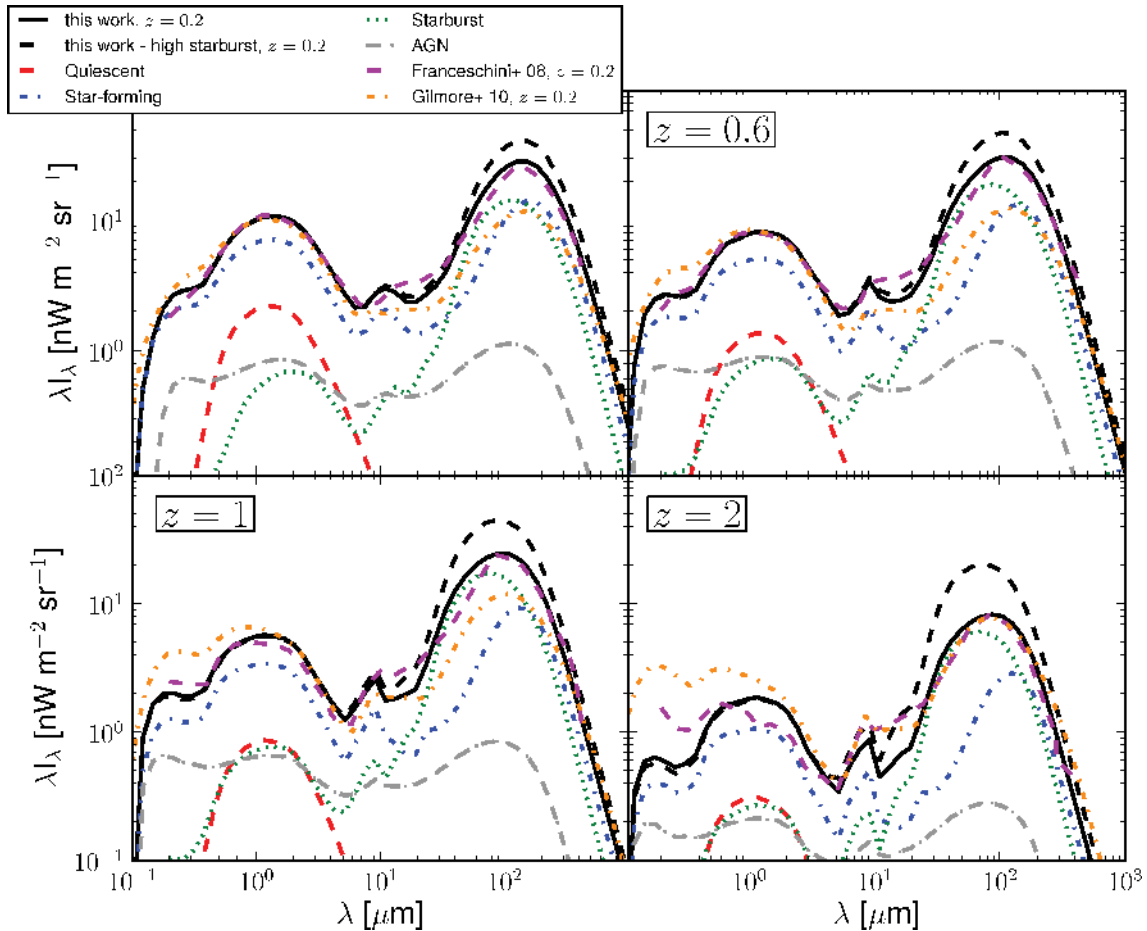
Figure 14. EBL in a comoving frame predicted by our model at different redshifts for the two assumptions for the extrapolation of the fractions for $z > 1$ (see Section 4.1). The contribution to the EBL from quiescent (dashed red line), star-forming galaxies (dot–dashed blue line), starbursts (dotted green line) and AGN galaxies (dot–long-dashed grey line) to the *fiducial* model is shown. For comparison, the predictions from other models are shown using a dashed magenta line for FRV08 and a dot–dashed orange line for GSPD10.

Table 4. Contribution from the different galaxy populations to the bolometric intensity of the EBL at different redshifts in a comoving frame as defined by equation (11) to the *fiducial* extrapolations (see Section 4.1).

| z	Quiescent	Star-forming	Starburst	AGN	I_{bol} (nW m^{-2} sr^{-1})
0.0	4.71 (7 per cent)	39.70 (57 per cent)	20.45 (30 per cent)	4.41 (6 per cent)	69.26
0.2	3.86 (5 per cent)	38.96 (54 per cent)	24.54 (34 per cent)	5.25 (7 per cent)	72.60
0.6	2.35 (3 per cent)	31.98 (44 per cent)	31.94 (44 per cent)	5.77 (8 per cent)	72.05
1.0	1.46 (3 per cent)	21.66 (38 per cent)	28.97 (51 per cent)	4.36 (8 per cent)	56.46
2.0	0.51 (3 per cent)	6.46 (36 per cent)	9.87 (54 per cent)	1.34 (7 per cent)	18.18

γ-ray photons travelling across cosmological distances and EBL photons (see Nikishov 1962; Gould & Schréder 1966).

Blazars are an important source of extragalactic γ-ray emission and have become a relevant tool for indirectly measuring the EBL. These objects are believed to be an extreme category of AGNs. Their emission, which occurs at all wavelengths of the electromagnetic spectrum, comes from supermassive black holes (with masses of $\geq 10^7\,M_\odot$) swallowing matter accreted from their surroundings. In general, AGNs are characterized by a beamed emission perpendicular to the accretion disc known as jets, which are pointing towards us in the case of blazars.

The current theoretical models for the emission by this class of objects are of two kinds: leptonic or hadronic. Both models predict a spectrum with two peaks. The first peak is localized from radio to X-rays due to synchrotron radiation from relativistic electrons (leptonic model) or protons (hadronic model). However, the second peak has a different nature. This is because of the inverse Compton (IC) scattering of the same population of electrons that produce the synchrotron peak in the leptonic model (Böttcher 2007) whereas in the hadronic model, nuclear photodisintegration is advocated to explain the second peak (Sikora et al. 2009). Both models face serious difficulties in explaining intrinsic (i.e. EBL-corrected) VHE power-law indices harder than 1.5 and fail to explain slopes harder than 2/3. The intrinsic spectrum is the one that we would observe if there were no effect from the EBL.

The Energetic Gamma-Ray Experiment Telescope (EGRET) satellite observed AGNs in the local universe (hence not very attenuated), claiming that all of them have spectral indices $E^{-\Gamma_{\text{int}}}$
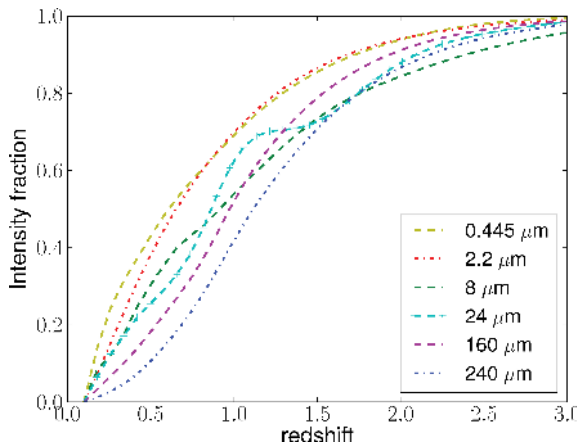
Figure 15. Buildup of the EBL at different wavelengths normalized to $z = 0.1$. For example, according to the *fiducial* model ∼70 per cent of the local EBL at 2.2 μm comes from $z < 1$, but only ∼40 per cent of the local EBL at 240 μm.
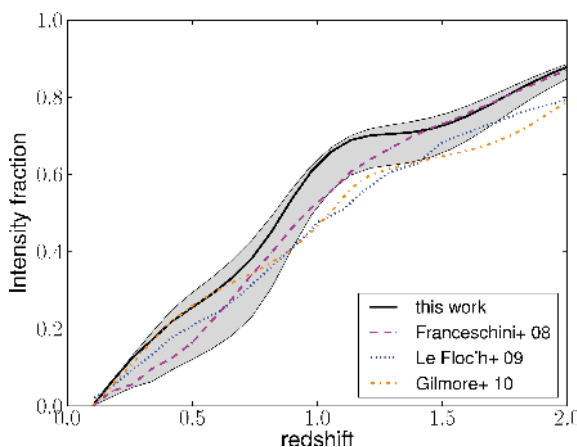
Figure 16. Buildup of the EBL at 24 μm obtained from different phenomenological models, normalized to $z = 0.1$, compared with the *Spitzer*/MIPS data by LeFloc'h et al. (2009). For example, according to our *fiducial* extrapolation (see Section 4.1), about 75 per cent of the local EBL at 24 μm was already in place at $z \sim 1.5$. Uncertainties in the modelling are shown with a shadow region (see Fig. 13). The curve from FRV08 has been calculated by us from their published EBL densities.

with $\Gamma_{\text{int}} \geq 1.5$ being in the high-energy (30 MeV–30 GeV) regime (Hartman et al. 1999). This result has been confirmed by the Fermi Collaboration (within uncertainties), which has published a catalogue of AGNs detected by the *Fermi* Large Area Telescope all-sky survey during its first year in operation (Abdo et al. 2010a). From this observational fact, and the above theoretical issues, it is usually conservatively considered that no AGN could have an intrinsic VHE spectrum fitted by a power law with an index harder than 1.5. Some authors such as Katarzyński et al. (2006), Stecker, Baring & Summerlin (2007), Böttcher, Dermer & Finke (2008) and Aharonian, Khangulyan & Costamante (2008) provide some mechanisms within standard physics to reach slopes harder than 1.5, but never harder than $\Gamma_{\text{int}} = 2/3$.

The EBL may be constrained using VHE observations of extragalactic sources if their intrinsic emitted spectra are known. As mentioned in Section 1, γ-ray photons coming from cosmological distances are attenuated by photon–photon pair production by EBL photons. The cross-section of this reaction depends on the product

shown in the left-hand side of equation (12):

$$\sqrt{2\varepsilon E(1 - \cos\theta)} \geq 2m_{\text{e}}c^2 \tag{12}$$

$$\varepsilon_{\text{th}} \equiv \frac{2m_{\text{e}}c^2}{E(1 - \cos\theta)}, \tag{13}$$

where, in the rest frame at redshift z, E is the energy of the γ photon, ε is the energy of the EBL photon and θ is the angle of the interaction, which defines an energy threshold ε_{th} for the EBL-photon energy given in equation (13) with m_{e} being the electron mass.

The cross-section peaks at about twice ε_{th}, which produces a peak in the interaction at $\lambda\,(\mu m) = 1.24E$ (TeV). From this property, a γ-ray with an energy of 1 TeV interacts mainly with a photon of the EBL with a wavelength of ∼1 μm. The details may be found, for example, in Madau & Phinney (1996).

For a given observed spectrum of a source at redshift z, we can find the intrinsic spectrum by assuming a particular EBL model and multiplying by the attenuation factor to *de-absorb* the spectrum using equation (14), i.e.

$$\left.\frac{\mathrm{d}F}{\mathrm{d}E}\right|_{\text{int}} = \left.\frac{\mathrm{d}F}{\mathrm{d}E}\right|_{\text{obs}} \exp\left[\tau(E, z)\right], \tag{14}$$

where the subscript obs means observed, int is intrinsic and $\tau(E, z)$ is the optical depth dependent on the observed energy E of the γ photon for a given EBL-photon density and redshift:

$$\tau(E, z) = \int_0^z \left(\frac{\mathrm{d}l'}{\mathrm{d}z'}\right)\mathrm{d}z' \int_0^2 \mathrm{d}\mu\frac{\mu}{2} \int_{\varepsilon_{\text{th}}}^\infty \mathrm{d}\varepsilon'\,\sigma_{\gamma\gamma}(\beta')n(\varepsilon', z') \tag{15}$$

$$\beta' = \frac{2m_{\text{e}}^2c^4}{E\varepsilon\mu(1 + z)^2}, \tag{16}$$

where $\mathrm{d}l'/\mathrm{d}z' = c|\mathrm{d}t'/\mathrm{d}z'|$ is given by equation (8), $\mu = 1 - \cos\theta$, $\sigma_{\gamma\gamma}$ is the photon–photon pair production cross-section, β' is given by equation (16) and n is the proper number density per unit energy of EBL photons.[5] We show in Fig. 17 the optical depth and attenuation for sources at $z = 0.1, 0.3, 0.6$ and 1.

Since the EBL produces an attenuation of the VHE spectra, a mere detection of VHE photons (using some constraint on the intrinsic blazar power spectrum) places an upper limit on the EBL density. Some upper limits have been derived by different authors, fitting EBL models to the density level where the condition $\Gamma_{\text{int}} = 1.5$ is satisfied, building *ad hoc* EBL models. We plotted these limits in Fig. 13 (Aharonian et al. 2006; Mazin & Raue 2007; Albert et al. 2008). Each of these upper limits comes from the study of different blazars with a different measured energy spectrum. Due to the peak of the interaction previously mentioned, each of the studies constrains different ranges on the EBL. Aharonian et al. (2006) used the VHE spectrum of the blazar 1ES 1101−232 at $z = 0.186$ observed from 0.2 to 3 TeV, scaling the model by Primack et al. (2001) multiplying the total EBL intensity by a constant to satisfy the $\Gamma_{\text{int}} = 1.5$ condition. Albert et al. (2008) used the spectrum of 3C 279 at $z = 0.536$ observed from 0.08 to 0.5 TeV, scaling a slightly modified model by Kneiske et al. (2002). Mazin & Raue (2007) used a compilation of blazars at different redshifts and observed at different energies, and splines from a grid as EBL densities. They made two different assumptions about the maximum Γ_{int} leading to two different upper limits (called *realistic* and *extreme* by the authors).

---

[5] Attenuation files are publicly available at http://side.iaa.es/EBL/
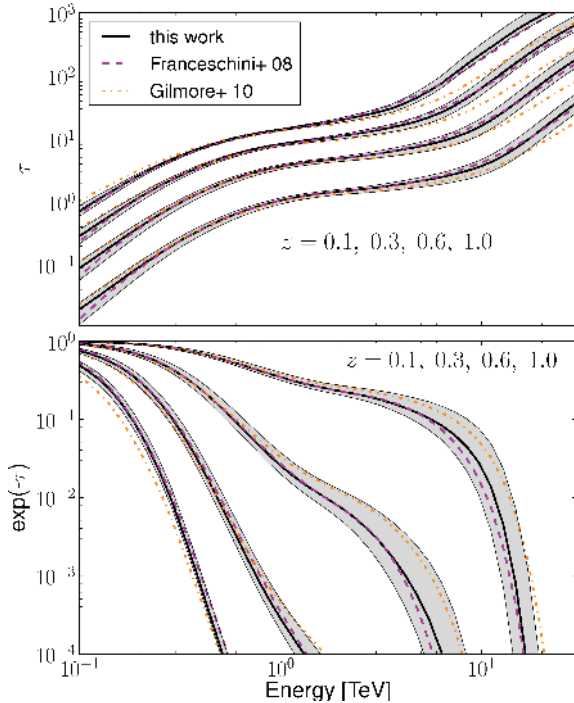
Figure 17. *Upper panel*: optical depth versus observed energy of γ-ray photons for sources at different redshifts (from bottom to top $z = 0.1, 0.3, 0.6$ and 1), due to the EBL computed for our model in a solid black line, for FRV08 in a dashed magenta line and for GSPD10 in a dot–dashed orange line. *Lower panel*: flux attenuation versus observed energy of γ-ray photons for fictitious sources at different redshifts (from right to left $z = 0.1, 0.3, 0.6$ and 1). We have calculated attenuation for the FRV08 and GSPD10 models using the EBL data provided by the authors. The EBL uncertainties in Fig. 13 are propagated to the optical depth and flux attenuation. They are shown here with a shadow region.

We see in Fig. 13 that the *fiducial* EBL model (hereafter all the results in this section are discussed for this, unless otherwise stated) is below the upper limits at all wavelengths, except at the largest wavelengths, where it slightly exceeds the limits from the *realistic* case by Mazin & Raue (2007). This fact is discussed in Section 5.2.1 and it is explained why we do not consider this a major problem. Another limit not plotted comes from the blazar 1ES 0229+200 at $z = 0.140$ (Aharonian et al. 2007). Its study sets a lower limit in the slope of the local EBL spectrum between 2 and 10 µm, $\alpha \geq 1.10 \pm 0.25$, to satisfy the limit on AGN's spectra $\Gamma_{int} \geq 1.5$. We remark that they set the limit only on the slope, not on the intensity level. We have fitted our model in that wavelength range to a power law $\propto \lambda^{-\alpha}$ obtaining $\alpha = 1.19 \pm 0.07$. Our model is thus compatible with this constraint.

It is also possible to set upper limits on the unknown redshift of blazars assuming an EBL model and finding the redshift by which the EBL-corrected spectrum satisfies $\Gamma_{int} = 1.5$ (Prandini et al. 2010; Yang & Wang 2010). We apply this method to the PG 1553+133 spectrum observed by MAGIC (Albert et al. 2007), assume an EBL-corrected spectrum given by a power law and find an upper limit at $z \leq 0.85 \pm 0.07$ in agreement with the lower limit ($z \geq 0.4$) found by Danforth et al. (2010) using absorption features in the Lyα forest of the blazar.

As shown in Fig. 17, our EBL model implies the same attenuation as other recent models we compare to over all the energy range observed by the current generation of IACTs. Larger transparency than the observationally based model by FRV08 is found (roughly

a factor of ~2 in flux, but still within the uncertainties) for γ-ray photons with energies between ~6 and 15 TeV for $z \sim 0.1$, but a factor of ~2 in flux less transparent than the GSPD10 theoretical approach around ~10 TeV. For the high-redshift case, our model predicts the same attenuation as FRV08, but a factor of ~1.5 more transparency than GSPD10 for sub-TeV energies. Note that a small difference in the optical depth has large effects on the spectra due to the exponential in equation (14); for example, a factor of 1.5 in optical depth leads to a factor of ~5 in attenuation.

5.2 Application to extreme known blazars

We now proceed to test whether the observed spectra of the three most constraining AGNs known in the VHE range due to their hard spectra, or due to their large redshift, satisfy the condition that the intrinsic spectrum corrected by the attenuation derived with our model has $\Gamma_{int} \geq 1.5$. We consider the blazars: Mrk 501 at $z = 0.034$ detected by the HEGRA system of Cherenkov telescopes in 1997 (Aharonian et al. 1999, with a re-analysis by Aharonian et al. 2001), Flat Spectrum Radio Quasar (FSRQ) 3C 279 at $z = 0.536$ observed by MAGIC (Albert et al. 2008) and the blazar 3C 66A observed by VERITAS at $z = 0.444$ (Acciari et al. 2009), all of them seen in a flaring state. All these blazars are plotted in Fig. 18, showing in the legends that the condition $\Gamma_{int} \geq 1.5$ is satisfied.

5.2.1 Mrk 501

The highest energy bins in this measurement, where a significant deviation from a power law is observed (see the upper-left panel of Fig. 18), are affected by the far-IR EBL at $\lambda > 60$ µm. This is the region of the EBL spectrum where a disagreement with the *realistic* (but not *extreme*) upper limits of Mazin & Raue (2007) was found. The problem comes from the very low statistics and high systematic uncertainties at such high energies (Aharonian et al. 1999). A later re-analysis of the same observation done in Aharonian et al. (2001) accounts for larger systematic uncertainties as shown in the upper-right panel of Fig. 18.

This exponential behaviour for the highest energy bin was already observed from the first EBL models (e.g. Malkan & Stecker 1998; Primack et al. 1999; Kneiske et al. 2002), whose EBL levels were higher than the more recent ones. This fact was discussed thoroughly in Dwek & Krennrich (2005), and even some exotic explanations such as Lorentz invariance violation (Stecker & Glashow 2001) were proposed. More recent EBL models with a more transparent universe (such as our model, FRV08 and GSPD10) relax such predictions. The solutions to exponential spectra and photon pile-up could involve widespread problems with the photon statistics and systematic uncertainties in the observations (as the results from the later re-analysis suggests), or new mechanisms extending the normal synchrotron self-Compton (SSC) model, using external regions close to the γ-ray source with target photons. The EBL uncertainties in the far-IR leading to the attenuation uncertainties at these high energies, as shown in Fig. 18, might contribute to the solution as well.

Another observed flare with better statistics with the current generation of IACTs up to such high energies as ~20 TeV would be very helpful in constraining these possibilities.

5.2.2 3C 279

Fig. 18 shows in the lower-left panel the EBL-corrected VHE spectrum for this source. An external photon field providing target
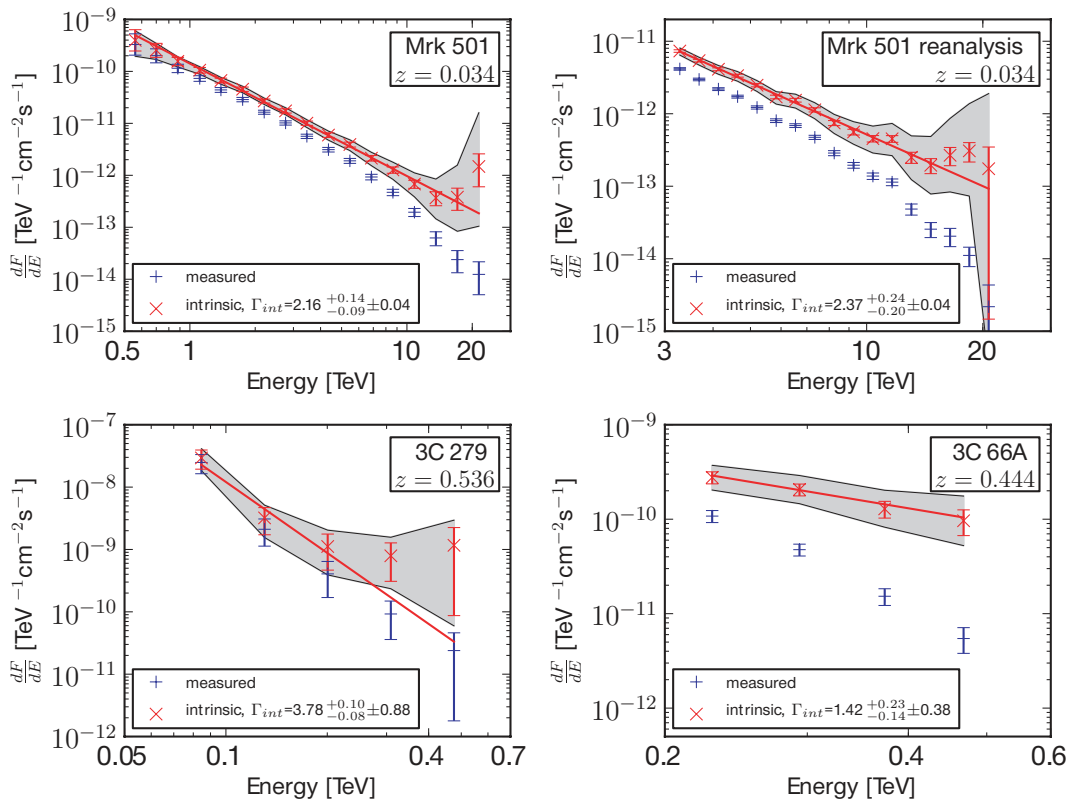
Figure 18. VHE spectra measured (blue) and EBL corrected from the attenuation calculated with our EBL model (using the *fiducial* extrapolation for the galaxy-SED-type fractions at $z > 1$, in red) of three extreme blazars: Mrk 501 observed in a very high state up to energies larger than 20 TeV (upper-left panel; Aharonian et al. 1999) and a re-analysis of the same data (upper-right panel; Aharonian et al. 2001); 3C 279, a flat-spectrum radio quasar with the highest redshift ($z = 0.536$) ever detected for a VHE γ-ray source (lower-left panel; Albert et al. 2008); and 3C 66A, a BL Lac with probably (because its redshift $z = 0.444$ is not very secure) the highest redshift ever detected for an object of this class (lower-right panel; Acciari et al. 2009). Uncertainties from the EBL modelling as well as statistical and systematic errors are shown with a shadow region. The straight red line is the best-fitting power law for every blazar with index Γ_{int}. The first uncertainties in the index are due to the EBL modelling as shown in Fig. 17 and the second uncertainties are statistical plus systematic errors in all blazars, except 3C 66A where only statistical errors are shown.

photons for IC (such as that provided by a broad-line emission region) might be necessary to explain the flat behaviour at the largest energy bins, as discussed in Albert et al. (2008). Instrumental systematic uncertainties might explain this behaviour as well. We note here that our model is already matching the lower limits from galaxy counts at the wavelengths where γ-ray attenuation with the observed energies occurs, and a much lower EBL density than the one calculated in this work does not seem realistic. The attenuation uncertainties from the EBL modelling are too low at this redshift and these energies to explain that spectral behaviour.

5.2.3 3C 66A

Fig. 18 shows in the lower-right panel the EBL-corrected VHE spectrum for this source, whose EBL-corrected slope is well within the 1σ limit of the $\Gamma_{int} \geq 1.5$ according to the calculated intrinsic index. It is important to note that the redshift considered for this object is calculated using just one emission line and is thus not very secure (see discussion in Bramel et al. 2005), and its attenuation might be indeed overestimated if the redshift is lower than assumed.

5.3 Conclusions on the limits from blazars

It is concluded from the study of these extreme blazars that our EBL is generally compatible with the hardness of the EBL-corrected slopes expected from theoretical arguments. However, it is clear

that a simple SSC model cannot explain any flatness at the highest energies of the EBL-corrected spectra of either Mrk 501 or 3C 279, which suggests that some extension to the model may be necessary such as an external photon region, a better understanding of the IACT systematic uncertainties or even a revision of the propagation mechanisms mainly through the intergalactic medium (see Sánchez-Conde et al. 2009).

5.4 Propagation of the EBL uncertainties to the γ-ray attenuation

As shown in Fig. 17, the uncertainties in the attenuation are dependent on the observed γ-ray energy as well as the redshift: the higher the energy or the redshift, the higher the uncertainties in the attenuation. The attenuation uncertainties shown were calculated from the uncertainties in our EBL modelling, which were shown in Fig. 13, explained in Section 4 and will be thoroughly discussed in Section 6.1. For sub-TeV energies up to around 1 TeV, the uncertainties in the flux attenuation are never higher than a factor of $\sim$2 and generally lower. The uncertainties in the EBL-corrected spectra in this case are dominated by other effects (see indices in Fig. 18). For energies larger than 10 TeV, the uncertainties are around a factor of several. The uncertainties in the EBL-corrected spectra up to such high energies due to the EBL modelling are considerable. These high uncertainties are derived from the EBL in the far-IR

region due to the very fast increment of the EBL-photon density (n, see equation 15) with longer wavelengths. Observations of sources at low redshift but energies larger than ~ 10 TeV will set constraints on these uncertainties.

6 DISCUSSIONS AND COMPARISON WITH SEMI-ANALYTIC MODELS

6.1 Discussion on EBL uncertainties

As explained in Section 3, we adopt a lower limit to the photometric errors higher than those in the AEGIS catalogue. Different lower limits are set from 1 to 10 per cent of the photometric measurements. That is, if the error in any band is lower than our limit then we set it to the limit. The results are sensitive to the limit choice in R and I (where the errors in the catalogue are the lowest), but not for the other bands. The galaxy-SED-type fractions change for lower limits of 1–6 per cent, but there is little change if the level is set higher than 6 per cent. The change is mostly for the quiescent and star-forming galaxy fractions. If we use the errors in the catalogue without any change, we find 10 per cent more quiescent galaxies at $z = 0.3$ than for a lower limit of 6 per cent, which decreases to ~ 3 per cent more quiescent galaxies at $z = 0.9$ than for a lower limit of 6 per cent, as shown in Fig. 8. The change is mostly in Ell2-type galaxies, according to the SWIRE classification. We have investigated those quiescent galaxies that change their best fit to star-forming galaxies upon raising the lower limit on the errors and find that they are often fitted much better by a star-forming SED. In many cases they even have detection in MIPS 24, clearly indicating ongoing star formation. On the other hand, based on the comparison of our photometric measurements to those of other catalogues we estimate that any error in the photometry lower than ~ 5 per cent should not be considered very reliable. For these reasons, we set the lower limit at 6 per cent for the model. The uncertainties due to this are below the *fiducial* model in Fig. 13, and for the reasons stated an EBL in this region should not be considered very likely (and therefore neither its derived attenuation in Fig. 17).

Another source of uncertainty accounted for in Figs 8 and 13 is the $\chi^2_{\rm red}$ cut that separates good and bad SED fits. The main change occurs for AGNs, where for a relaxation in the cut (from $\chi^2_{\rm red} = 10$ to 20), the fraction can increase by as much as 10 per cent at $z = 0.9$ and by a smaller fraction at $z = 0.3$. These changes affect the EBL in the following way: higher AGN fractions increase the UV as well as the mid-IR, while higher quiescent fractions decrease the flux at these wavelengths. This effect affects the uncertainties above the *fiducial* model, and an EBL intensity in this shadow region is considered more reliable than in the region below the *fiducial* model (the same as its derived attenuation in Fig. 17). While $\chi^2_{\rm red}$ cuts do not have an appreciable effect on the far-IR flux, there is a substantial change arising from the choice of extrapolation in SED types above $z \sim 1$, as we find in the *high-starburst* assumption. Fig. 13 also accounts for the uncertainties in the Schechter parameters of the LF given by C10 but these are small.

Two major potential problems for our modelling might be a colour-dependent selection effect and the extrapolation of the galaxy-SED-type fractions for $z > 1$. It was already shown in Section 2.2 that the colour-selection effect is rather small. From the fact that most of the light in the EBL comes from the knee of the LF around $L_\star$, where our sample does not suffer any colour-dependent selection effect, we do not consider this to be a significant problem for our EBL calculation. Our estimated galaxy-SED-type fractions appear to be consistent with works of others as well. For example,

our results agree with Blanton (2006) and Faber et al. (2007), who find roughly no evolution for late-type (blue) galaxies from $z \sim 1$ to 0 within a 10 per cent range and an increment of the early type (red) population in the same redshift range by at least a factor of 2. We also highlight that the galaxy-SED-type fractions that we calculated for the local universe smoothly link with our independently derived results at $z \sim 0.3$.

Regarding the galaxy-SED-type fraction extrapolations, we have considered two rather different approaches which basically lead to the same evolving luminosity densities and EBL for the optical/near-IR range where γ-ray attenuation occurs, as shown in Figs 11 and 14, respectively. This fact is due to the shape of the stellar emission, because the contribution to the optical/near-IR peak is very similar for quiescent, star-forming and starburst galaxies for a given M_K. We recall here that the normalization to our model is fixed by the rest-frame K-band LF by C10. The only difference between our extrapolations is at the far-IR peak, where our results are considered to be less robust for this reason as well as for the reasons stated below regarding the SWIRE templates and the lack of photometric data. Deeper observations by future galaxy surveys will help in characterizing the galaxy-SED fractions up to higher redshifts.

It was also checked how the fractions change if the detection limit is relaxed from 5σ to 3σ for the bands where there are observations, but no detections. Many more quiescent galaxies than in the 5σ case were found, even a factor of larger than 2, due to the low detection limit on the MIPS 24 instrument, but generally they are not good fits.

In our work, we have not differentiated between the spectroscopic and secure photometric redshifts. This is an approximation, and it is necessary to check that this is consistent with our results. We find that the galaxy-SED-type fractions derived from both sub-catalogues are clearly compatible and the trends are the same.

Galaxies fitted to a starburst SED may instead be very late-type star-forming galaxies (or vice versa), because both SED templates are rather similar in the regions where we have data. This may be called mis-typing and its effect is expected to be larger for faint galaxies, because the major fraction of faint galaxies is star-forming or starburst and not massive quiescent or AGN galaxies. Such small galaxies are probably rather metal poor and thus lack dust. Hence, their SEDs are probably more like star-forming galaxies rather than starbursts (in agreement with our results in Fig. 9). It is a source of uncertainty in the mid- and far-IR (underestimating or overestimating light) and might explain the excess found in Figs 11 and 12 compared with the data. Far-IR data would help in resolving this issue, but the number of galaxies with detection in MIPS 70 is rather low to make statistical estimations. *Herschel* data will be very useful, thanks to their good spatial resolution and deep photometry in the far-IR.

Another source of uncertainties in our model that quantitatively we have not accounted for arises from the use of local SED templates to fit galaxies at $z > 0.3$. This comes from the fact that the SWIRE templates are based on observations of local galaxies, and we expect that they become worse fits when the redshift is increasing. This problem will be addressed by new data from WFC3 on *Hubble Space Telescope* (*HST*) and the next generation of ground and space optical/near-IR telescopes such as the *James Webb Space Telescope*.

The lowest EBL flux in Fig. 13 is given by the case with the highest number of quiescent galaxies and the lowest number of AGN galaxies, which corresponds to the case of using the low errors in the catalogue and our $\chi^2_{\rm red}$ cuts. The highest EBL flux occurs with fewer quiescent galaxies and the highest fraction of AGN galaxies. This is the case with the 6 per cent lower limit for the errors in

the photometry and without a χ^2_{red} cut. Using the lower limits from galaxy counts in the UV and in the optical, we may rule out at $>2\sigma$ the mixing of galaxy-SED-type fractions predicting the highest fractions of quiescent galaxies and fewest AGNs in Fig. 8. We do not consider the VHE observations to exclude the models with higher far-IR, because the discrepancy is for wavelengths longer than 60 μm where those limits may not be reliable for the reasons stated in Section 5. Further VHE observations might indeed constrain our galaxy-SED-type fractions.

Thus to recall, the EBL uncertainties from the UV up to the mid-IR are low enough to recover the spectra of γ-ray sources with energies lower than ~ 10 TeV, but the EBL uncertainties have to be reduced in the far-IR (for neglecting uncertainties due to the EBL modelling) to correct higher energy sources. Additional photometry is needed there for clearly distinguishing between star-forming and starburst galaxies, and therefore for reducing the mis-typing, as well as for a better understanding of the far-IR region of the galaxy SEDs at $z > 0.3$. Characterizing the galaxy-SED-type fractions at $z > 1$ will reduce these uncertainties in the far-IR as well.

6.2 Discussion of the results

The local luminosity density from galaxies is observationally well constrained over all wavelengths from 0.1 to 1000 μm. As shown in Fig. 10, the prediction of the local luminosity densities is in very good agreement with observational results.

Fig. 11 showed the evolving rest-frame UV luminosity density. These results agree well with the observational data by Gabasch et al. (2006) and Dahlen et al. (2007) within uncertainties, but they are a factor of ~ 1.6 below the data for $z = 1.7$ and 2.2. In Fig. 11, the evolution of the rest-frame luminosity in the K band from our calculations is compared to that of the independent observational works. Some disagreement was found in the case of Barro et al. (2009) that might be explained by the fact that they do not correct their sample for incompleteness and only consider the brightest sources, unlike the LF by C10. Therefore, their results should be considered as lower limits. The direct comparison in Fig. 11 with the rest-frame luminosity density in the B band shows that our luminosity in this band is not in contradiction to other independent works. We are doing really well reproducing the data from Norberg et al. (2002), Gabasch et al. (2004) and Ilbert et al. (2005). We might be indeed overestimating the light in this band by 15–20 per cent for $z < 1$ according to the data by Faber et al. (2007) and by a factor of ~ 2 for $z > 1$ according to the data by Dahlen et al. (2005), but the latter does not significantly affect our results for the local EBL because as shown in Fig. 15, most of the optical/near-IR light comes from $z < 1$. The comparison of the bolometric IR luminosity density with that of the observational works by FRV08 and Rodighiero et al. (2010) is very good, even though we are a factor of ~ 2 higher around $z \sim 1$.

A good agreement was found with the upper envelope of the data cloud on the calculations for the SFR history from $z \sim 1.5$ down to the local universe using equation (6) (see Fig. 12), using our *fiducial* extrapolation. According to Magnelli et al. (2009) at around $z \sim 1$ the main contributor to the star formation is the obscured IR contribution, instead of the UV. We may be overpredicting some of this obscured IR light around $z \sim 1$ due to the lack of far-IR photometric data in our galaxy catalogue that allow a clear classification between late star-forming and starburst galaxies as discussed in Section 6.1. With the *high-starburst* extrapolation of the galaxy-SED-type fractions was checked that increasing the starburst-like population a factor of ~ 3 from $z \sim 1$–2, we may get a flatter SFR

density history up to $z \sim 2$, but even higher than the observational data. This *high-starburst* assumption does not change our general picture of the local EBL, but increases the far-IR peak by a factor of ~ 1.5 (as is considered in Fig. 13 and shown explicitly in Fig. 14 for some other redshifts).

The EBL calculated in this work matches the data from galaxy counts from the UV up to the mid-IR (see Fig. 13), except the data found in Levenson & Wright (2008). Higher intensities than the data from galaxy counts were calculated in the far-IR but in agreement with direct detections. The EBL evolution shown in Fig. 14 is in good agreement with FRV08 up to $z = 1$. At higher redshift, our results are different in the UV and optical/near-IR. This may be due to the fact that FRV08 extrapolate the galaxy evolution, while in our model this evolution is entirely based on the observed LF by C10 up to $z = 4$. See Section 6.3 for a comparison with the results by GSPD10.

There are some works in the literature where the contribution from AGN galaxies to the EBL is studied. According to recent works that focus in the mid-IR (e.g. Silva, Maiolino & Granato 2004; Matute et al. 2006), this contribution should not be larger than 10–20 per cent. This is in agreement with our results: we find that the AGN-galaxy contribution to the bolometric EBL is 6 per cent for the *fiducial* extrapolation (Table 4) and 13 per cent for the case with the largest AGN fraction in Fig. 8. For the wavelength range between 1 and 20 μm, the AGN contribution from our model is also between 8 and 16 per cent. We estimate that this contribution to the comoving bolometric EBL slightly increases with redshift.

The EBL buildup is studied in Figs 15 and 16. It is found that most of the local UV/optical/near-IR EBL is built up at $z < 1$, while the far-IR EBL is mostly built up at $z > 1$. This result for the far-IR light agrees well with the observational work by Devlin et al. (2009), but disagrees with Chary & Pope (2010). In any case, our uncertainties in the far-IR are very large. Differences of up to 40 per cent were found in the buildup of the local EBL at 24 μm. These differences are due to the fact that a very small change in the mid-IR region leads to a very strong difference in this buildup plot and due to the mid-IR peak that we get at larger redshifts (see Fig. 14) because of the shape of the galaxy SEDs. We point out here that the EBL buildup is on how the light is being built up, and not about the absolute intensity value.

We have already discussed our results on γ-ray attenuation in Section 5.

6.3 Comparison with SAMs

In this section we compare our EBL estimation against the EBL model described in SGPD10 and GSPD10, which is based on SAMs of galaxy formation. The comparison for γ-ray attenuation has been thoroughly discussed in Section 5. We notice that slightly different cosmological parameters were used for our model and that by SGPD10. The latter uses the latest values from *Wilkinson Microwave Anisotropy Probe* 5, which slightly affect all the results in the local universe as well as their evolution.

We already saw in Fig. 11 the comparison between our observational luminosity densities and the theoretical prediction by SGPD10 for the comoving luminosity density versus redshift in the UV, in the near-IR (K band), in the optical (B band) and for the bolometric IR luminosity. We note that our K-band luminosity density evolution is given exclusively by the C10 LF, because at that band our choice of galaxy-SED fractions does not affect our results. This quantity is above the prediction by SAMs by a factor of around 20 per cent from $z \sim 2$ down to the present universe. The UV from

this SAM is above our results for all redshifts, except at $z \sim 1$. At $z \sim 2$, it is a factor of 4 higher. For the *B*-band luminosity density, the agreement is excellent from $z \sim 1$ down to the local universe. For $z > 1$, SAMs predict a factor of several more light than our observationally based approach. We may see the consequences of this for the EBL evolution in Fig. 14 for high redshifts where the excess of light has not been diluted by the expansion of the universe. For the bolometric IR luminosity, SAMs seem to systematically predict at least a factor of ~ 2 less light than our calculations and the one by FRV08. This difference is maximized around $z \sim 1$ up to a factor of ~ 4.

Fig. 12 showed a comparison between our SFR density estimation and that predicted by SGPD10 as calculated by using equation (6). From $z \sim 3$–1 our SFR densities have a different behaviour: for our observational model increases up to $z = 1$ and for SGPD10 keeps constant down to $z \sim 1.7$. For lower redshifts, both models decline down to the local universe.

In general, a very good agreement between the local EBL from the UV up to the mid-IR predicted by our method and the SAM of SGPD10–GSPD10 is seen in Fig. 13. A factor of ~ 1.5 higher intensity is found in the local UV from SAMs, and around the same factor lower intensity around 15 μm. For the far-IR peak, the difference comes from the different templates used for the dust component in the far-IR, which is given by the GRASIL code in the case of the SWIRE templates (which we use) and by a interpolation between the observed 70 and 160 μm by MIPS in the case of the templates used by these SAMs (Rieke et al. 2009).

The agreement on the evolution is very good as well as seen in Fig. 14, even though at high redshift ($z > 2$), GSPD10 predicts a factor of several more light in the UV. This is due to galaxies within the faint end of the theoretical LF at $z > 2$. We recall that our observational model seems to already be overproducing light in the *B* band for $z > 1.5$ according to data in Dahlen et al. (2005) (see Fig. 11).

6.4 Overview on the cosmological picture

The evolutionary path that we have in mind to interpret the evolution of the galaxy-SED-type fractions is as follows: AGNs are mostly formed by mergers between galaxies during the hierarchical growth of dark matter haloes (e.g. Hopkins et al. 2009). When the merging galaxies are gas rich (also known as wet mergers), inflows of gas are produced leading to starburst galaxies and to the mass growth of the central black hole. The central black hole activity begins to expel the gas. Eventually, the gas is exhausted, switching off the AGN. The galaxy continues forming stars as a star-forming galaxy until the gas is fully depleted and then becomes a quiescent galaxy (Hopkins et al. 2008a,b).

It is now a well-known observational fact that galaxies are bimodal in some properties such as colours (Strateva et al. 2001; Blanton et al. 2003b). They group in two different regions in colour–magnitude diagrams defining the red sequence and the blue cloud. Galaxies forming stars are in the blue cloud. Some galaxies have their star formation quenched when they become satellite galaxies in a larger halo; they cease to accrete gas and join the red sequence. Central galaxies form in the blue cloud, but they join the red sequence when they form a supermassive black hole and/or their halo mass exceeds approximately 10^{12} M$_\odot$ and/or they become satellite galaxies in a cluster. The most massive red galaxies cannot simply be quenched central blue galaxies, since the latter are not massive enough; thus they must have been created by mergers without much star formation (also known as dry mergers). This effect is shown in

Fig. 4, taking into account that the *K*-band absolute magnitude M_K is a good tracer of the galaxy stellar mass, as shown in Brinchmann & Ellis (2000).

Massive galaxies today (very bright M_K) form their stars first, which is known as *downsizing* (Cowie et al. 1996; Pérez-González et al. 2008). This initially seemed at odds with the hierarchical nature of the ΛCDM paradigm, in which small haloes form first and agglomerate into larger ones. But the idea that star formation is efficient only in dark matter haloes with a narrow range of masses naturally explains how the phenomenon of downsizing arises: haloes that are massive today passed through the star-forming mass band between 10^8 and 10^{12} M$_\odot$ earlier and thus formed their stars earlier than haloes that are less massive today (Conroy & Wechsler 2009; Croton 2009).

A careful examination of Fig. 4 reveals some interesting trends. We find that all the oldest galaxies (~ 13-Gyr old, Ell13) are in the red sequence. However, the younger quiescent galaxies (~ 5-Gyr old, Ell5) can be found in the red sequence as well as in the green valley (the region between the red sequence and the blue cloud). For the youngest quiescent galaxies (~ 2-Gyr old, Ell2) we find that for $z > 0.6$ they populate the green valley, while for $z < 0.6$ they belong to the blue cloud. All the early type star-forming galaxies (S0, Sa) are in the red sequence. Later type star-forming galaxies such as Sb and Sc start to populate the green valley as well as the red sequence. Most of the very late-type star-forming galaxies (Sd, Sdm, Spi4) populate the blue cloud. Starburst galaxies are mainly in the green valley, but some of them are in the bluer region of the red sequence and in the redder region of the blue cloud. The same happens to AGNs, but they tend to be in the blue cloud more than in the red sequence.

We note that the increasing rate of quiescent galaxies as z declines is roughly the same as the decreasing rate of starburst-type galaxies from $z \sim 0.9$ to 0.7. One possible explanation would be the transformation of starbursts (either merger or huge-cold-gas reservoir triggered) directly to quiescent galaxies, without an intervening stage of significant star formation. Another explanation is that the characteristic time in which starburst-like galaxies consume their cold gas is the same as that in which star-forming galaxies consume their lower cold-gas reservoir. Thus the specific SFRs of these populations are different, but the rate at which starbursts enter the star-forming sequence is the same as the rate at which star-forming galaxies become quiescent. From $z \sim 0.7$ to 0.3 the fraction of starbursts is very low, so the constant increase of the red sequence is modelled as due to AGNs preventing gas from cooling and forming stars.

7 SUMMARY AND CONCLUSIONS

A novel, robust and powerful method based on observations to derive the evolving spectrum of the EBL between 0.1 and 1000 μm is presented. This model is based on the observed rest-frame *K*-band galaxy LF over redshift by C10, combined with an estimation of galaxy-SED-type fractions based on a multiwavelength sample of ~ 6000 galaxies from AEGIS. This model has the following main advantages over other existing EBL models: transparent methodology, reproducibility and utilizing direct galaxy data. The best available data sets are used (C10's LF and the AEGIS galaxy catalogue) observed over a wide redshift range. The galaxy evolution is directly observed in the rest-frame *K* band up to $z = 4$. Observed galaxies up to $z = 1$ from the UV up to 24 μm with SEDs of 25 different types (from quiescent to rapidly star-forming galaxies and including AGN galaxies) are taken into account in the same

observational framework. A study of the uncertainties to the model directly from the data (such as uncertainties in the Schechter parameters of the C10 LF and the errors in the photometric catalogue) is done, and their propagated uncertainties to the γ-ray attenuation is studied.

A brief comparison with results from other recent EBL models is made here: Stecker et al. (2006) estimate a local EBL in the UV which is a factor of several higher than ours and in contradiction to recent γ-ray observations (Abdo et al. 2010b). A comparison with FRV08's results is thoroughly presented in Section 4. In general, our results are in good agreement, despite the fact that our modelling are different. Finke et al. (2010) have five different models based on different parametrizations of the SFR density of the universe and IMFs. The local EBL from the UV to the near-IR is similar to ours for their models *C* and *E*. Kneiske & Dole (2010) claim to model a strict lower limit for the EBL. However, our results for the local EBL in the UV are lower than the calculation by Kneiske & Dole (2010), but are in agreement with the robust lower limits from galaxy counts in the UV by Madau & Pozzetti (2000) and Xu et al. (2005). In the near-IR, the model by Kneiske & Dole (2010) is not compatible with the lower limits by Keenan et al. (2010). Our observationally based approach is also thoroughly compared with the results from the SAM of galaxy formation by SGPD10 and GSPD10 in Section 6.3. Our EBL results are in general in good agreement at least for $z < 2$, even though this SAM predicts more light (by up to a factor of several) than our observational approach in the UV and a factor of $\sim$2–3 less light in the far-IR.

Our methodology provides a tool for calculating the EBL more accurately at the longest wavelengths when a better understanding of the far-IR galaxy SEDs, new photometry and deeper LFs at those wavelengths is available from the *Herschel Space Observatory*.

Two extrapolations of the galaxy-SED-type fractions to $z > 1$ were considered, showing that these assumptions only affect the far-IR. It was calculated that the population with SED features of quiescent local galaxies increases by a factor of $\sim$2 since $z \sim 1$. The star-forming population remains roughly constant, while the starburst-like population decreases very quickly from around $\sim$20 per cent at $z \sim 1$. The AGN-like population decreases slower than the starburst-like population from almost 20 per cent at $z \sim 1$ to just around 2 per cent at $z \sim 0.3$. Data from the future *James Webb Space Telescope* will help to determine the galaxy-SED-type fractions at $z > 1$.

A low intensity local EBL ($z = 0$) was found, matching the lower limits from galaxy counts up to $\sim$30 μm. For longer wavelengths, our model predicts higher intensities than the data from galaxy counts, in agreement with direct measurements.

Our results are also compatible with all the upper limits from γ-ray astronomy according to the standard framework for the propagation of VHE photons through the universe, even though to account for the highest energies detected by Aharonian et al. (1999) for Mrk 501 we have to assume a $\Gamma_{int} < 1.5$, appeal to statistical and systematic uncertainties on this VHE spectrum, or attenuation uncertainties due to uncertainties in the EBL for such high energies as discussed in Section 5.

The EBL uncertainties in far-IR leading to attenuation uncertainties of a factor of several for energies larger than $\sim$10 TeV need to be addressed by the current and next generation of IR telescopes providing new photometric data and a better understanding of the galaxy IR emission. γ-ray astronomy may constrain these uncertainties from a better understanding of the emission mechanisms at those high energies (helped with simultaneous multiwavelength

observations) and of the instrumental systematic uncertainties. Observations aimed to measure photons with energies higher than $\sim$10 TeV at $z < 0.3$ are encouraged.

It is worth mentioning that high-energy (30 MeV–30 GeV) γ-rays are detected by *Fermi* for $z \leq 2.5$ from AGNs (Abdo et al. 2010a) and for $z \leq 4.5$ (Abdo et al. 2009) from gamma-ray bursts (GRBs). The reasons for these high-redshift detections include a larger γ-ray flux at lower energies and a lower density of EBL target photons that can interact with these γ-rays. Understanding the evolution of the EBL at UV wavelengths is essential to interpreting observations of these high-redshift sources. New observations of AGNs as well as the first GRB detection in the VHE range would help to make new and stronger constraints on the EBL (see Gilmore, Prada & Primack 2010).

The universe, according to our observationally based model, is more transparent than the estimation from FRV08 (a factor of $\sim$2 in flux) for VHE photons coming from low-redshift sources ($z \sim 0.1$) for energies between $\sim$6 and 15 TeV, but still the uncertainties here from the EBL modelling are large (a factor of several). The same attenuation as FRV08 is estimated for other energies. For VHE photons coming from larger redshift sources ($z \sim 1$), roughly the same attenuation as FRV08 is estimated. Here the attenuation uncertainties (for energies available to γ-ray telescopes) due to the uncertainties on the EBL modelling are low in comparison with other effects. At these redshifts, the uncertainties on the EBL-corrected spectra are dominated by instrumental systematic uncertainties. We may conclude that it is not expected to observe any such high-redshift ($z \sim 1$) multi-TeV γ-ray photons from blazars with the current or even next-generation telescopes such as the Cherenkov Telescope Array (Doro 2009) or the Advanced Gamma-ray Imaging System (Buckley et al. 2008), but we indeed expect a promising future for sub-TeV detections at these high redshifts.

REFERENCES

Abdo A. A. et al., 2009, Sci, 323, 1688
Abdo A. A. et al., 2010a, ApJ, 715, 429

Abdo A. A. et al., 2010b, preprint (arXiv:1005.0996)
Acciari V. A. et al., 2009, ApJ, 693, L104
Aharonian F. et al., 1999, A&A, 349, 11
Aharonian F. A. et al., 2001, A&A, 366, 62
Aharonian F. et al., 2006, Nat, 440, 1018
Aharonian F. et al., 2007, A&A, 475, L9
Aharonian F. A., Khangulyan D., Costamante L., 2008, MNRAS, 387, 1206
Albert J. et al., 2007, ApJ, 654, L119
Albert J. et al., 2008, Sci, 320, 1752
Arnouts S. et al., 2002, MNRAS, 329, 355
Arnouts S. et al., 2007, A&A, 476, 137
Barmby P., Huang J.-S., Ashby M. L. N., Eisenhardt P. R. M., Fazio G. G., Willner S. P., Wright E. L., 2008, ApJS, 177, 431
Barro G. et al., 2009, A&A, 494, 63
Bell E. F., McIntosh D. H., Katz N., Weinberg M. D., 2003, ApJS, 149, 289
Bernstein R. A., 2007, ApJ, 666, 663
Berta S. et al., 2010, A&A, 518, L30
Béthermin M., Dole H., Beelen A., Aussel H., 2010, A&A, 512, A78
Blanton M. R., 2006, ApJ, 648, 268
Blanton M. R. et al., 2003a, ApJ, 592, 819
Blanton M. R. et al., 2003b, ApJ, 594, 186
Böttcher M., 2007, Ap&SS, 309, 95
Böttcher M., Dermer C. D., Finke J. D., 2008, ApJ, 679, L9
Bramel D. A. et al., 2005, ApJ, 629, 108
Brinchmann J., Ellis R. S., 2000, ApJ, 536, L77
Bruzual G., Charlot S., 2003, MNRAS, 344, 1000
Buckley J. et al., 2008, in Aharonian F. A., Hofmann W., Reiger F., eds, AIP Conf. Proc. Vol. 1085, High Energy Gamma-Ray Astronomy. Am. Inst. Phys., New York, p. 902
Calzetti D., Armus L., Bohlin R. C., Kinney A. L., Koornneef J., Storchi-Bergmann T., 2000, ApJ, 533, 682
Cambrésy L., Reach W. T., Beichman C. A., Jarrett T. H., 2001, ApJ, 555, 563
Cameron E., Driver S. P., Graham A. W., Liske J., 2009, ApJ, 699, 105
Chabrier G., 2003, PASP, 115, 763
Chary R.-R., Pope A., 2010, preprint (arXiv:1003.1731)
Chary R. et al., 2004, ApJS, 154, 80
Cirasuolo M., McLure R. J., Dunlop J. S., Almaini O., Foucaud S., Simpson C., 2010, MNRAS, 401, 1166 (C10)
Coil A. L., Newman J. A., Kaiser N., Davis M., Ma C.-P., Kocevski D. D., Koo D. C., 2004, ApJ, 617, 765
Conroy C., Wechsler R. H., 2009, ApJ, 696, 620
Conselice C. J., Bundy K., U V., Eisenhardt P., Lotz J., Newman J., 2008, MNRAS, 383, 1366
Cowie L. L., Songaila A., Hu E. M., Cohen J. G., 1996, AJ, 112, 839
Croton D. J., 2009, MNRAS, 394, 1109
Cuillandre J.-C., Luppino G., Starr B., Isani S., 2001, SF2A-2001: Semaine de l'Astrophysique Française. EdP-Sciences, Les Ulis, p. 605
Daddi E. et al., 2007, ApJ, 670, 156
Dahlen T., Mobasher B., Somerville R. S., Moustakas L. A., Dickinson M., Ferguson H. C., Giavalisco M., 2005, ApJ, 631, 126
Dahlen T., Mobasher B., Dickinson M., Ferguson H. C., Giavalisco M., Kretchmer C., Ravindranath S., 2007, ApJ, 654, 172
Danforth C. W., Keeney B. A., Stocke J. T., Shull J. M., Yao Y., 2010, ApJ, 720, 976
Davis M. et al., 2007, ApJ, 660, L1
Devlin M. J. et al., 2009, Nat, 458, 737
Dickinson M., FIDEL team, 2007, A&AS, 38, 822
Doro M. (for the CTA consortium), 2009, preprint (arXiv:0908.1410)
Driver S. P., Popescu C. C., Tuffs R. J., Graham A. W., Liske J., Baldry I., 2008, ApJ, 678, L101
Dwek E., Krennrich F., 2005, ApJ, 618, 657
Faber S. M. et al., 2003, in Masanori I., Moorwood A. F. M., eds, Proc. SPIE Vol. 4841, Instrument Design and Performance for Optical/Infrared Ground-Based Telescopes. SPIE, Bellingham, p. 1657
Faber S. M. et al., 2007, ApJ, 665, 265
Fardal M. A., Katz N., Weinberg D. H., Davé R., 2007, MNRAS, 379, 985
Fazio G. G. et al., 2004, ApJS, 154, 39

Finkbeiner D. P., Davis M., Schlegel D. J., 2000, ApJ, 544, 81
Finke J. D., Razzaque S., Dermer C. D., 2010, ApJ, 712, 238
Franceschini A., Rodighiero G., Vaccari M., 2008, A&A, 487, 837 (FRV08)
Frayer D. T. et al., 2006, ApJ, 647, L9
Gabasch A. et al., 2004, A&A, 421, 41
Gabasch A. et al., 2006, A&A, 448, 101
Gardner J. P., Brown T. M., Ferguson H. C., 2000, ApJ, 542, L79
Gehrels N., Michelson P., 1999, Astropart. Phys., 11, 277
Gilmore R. C., Prada F., Primack J., 2010, MNRAS, 402, 565
Gorjian V., Wright E. L., Chary R. R., 2000, ApJ, 536, 550
Goto T., Yamauchi C., Fujita Y., Okamura S., Sekiguchi M., Smail I., Bernardi M., Gomez P. L., 2003, MNRAS, 346, 601
Gould R. J., Schréder G., 1966, Phys. Rev. Lett., 16, 252
Hartman R. C. et al., 1999, ApJS, 123, 79
Hauser M. G., Dwek E., 2001, ARA&A, 39, 249
Hauser M. G. et al., 1998, ApJ, 508, 25
Hinton J. A., 2004, New Astron. Rev., 48, 331
Hopkins P. F., Hernquist L., Cox T. J., Kereš D., 2008a, ApJS, 175, 356
Hopkins P. F., Cox T. J., Kereš D., Hernquist L., 2008b, ApJS, 175, 390
Hopkins P. F. et al., 2009, MNRAS, 397, 802
Hopwood R. et al., 2010, ApJ, 716, L45
Huang J.-S. et al., , 2007, ApJ, 664, 840
Ilbert O. et al., 2005, A&A, 439, 863
Ilbert O. et al., 2006, A&A, 457, 841
Jones D. H., Peterson B. A., Colless M., Saunders W., 2006, MNRAS, 369, 25
Katarzyński K., Ghisellini G., Tavecchio F., Gracia J., Maraschi L., 2006, MNRAS, 368, L52
Keenan R. C., Barger A. J., Cowie L. L., Wang W.-H., 2010, preprint (arXiv:1008.4216)
Kennicutt R. C., Jr, 1998, ARA&A, 36, 189
Kneiske T. M., Dole H., 2010, A&A, 515, A19
Kneiske T. M., Mannheim K., Hartmann D. H., 2002, A&A, 386, 1
Kochanek C. S. et al., 2001, ApJ, 560, 566
Kriek M., van Dokkum P. G., Labbé I., Franx M., Illingworth G. D., Marchesini D., Quadri R. F., 2009, ApJ, 700, 221
Lagache G., Haffner L. M., Reynolds R. J., Tufte S. L., 2000, A&A, 354, 247
Lagache G., Puget J.-L., Dole H., 2005, ARA&A, 43, 727
Lawrence A. et al., 2007, MNRAS, 379, 1599
LeFloc'h E. et al., 2009, ApJ, 703, 222
Levenson L. R., Wright E. L., 2008, ApJ, 683, 585
Lorenz E., 2004, New Astron. Rev., 48, 339
Madau P., Phinney E. S., 1996, ApJ, 456, 124
Madau P., Pozzetti L., 2000, MNRAS, 312, L9
Magnelli B., Elbaz D., Chary R. R., Dickinson M., Le Borgne D., Frayer D. T., Willmer C. N. A., 2009, A&A, 496, 57
Malkan M. A., Stecker F. W., 1998, ApJ, 496, 13
Marchesini D. et al., 2007, ApJ, 656, 42
Matsumoto T. et al., 2005, ApJ, 626, 31
Matsuura S. et al., 2010, preprint (arXiv:1002.3674)
Mattila K., 2006, MNRAS, 372, 1253
Matute I., La Franca F., Pozzi F., Gruppioni C., Lari C., Zamorani G., 2006, A&A, 451, 443
Mazin D., Raue M., 2007, A&A, 471, 439
Menéndez-Delmestre K. et al., 2009, ApJ, 699, 667
Metcalfe L. et al., 2003, A&A, 407, 791
Montero-Dorta A. D., Prada F., 2009, MNRAS, 399, 1106
Morrissey P. et al., 2007, ApJS, 173, 682
Murphy E. J., Chary R.-R., Alexander D. M., Dickinson M., Magnelli B., Morrison G., Pope A., Teplitz H. I., 2009, ApJ, 698, 1380
Nikishov A. I., 1962, Soviet Phys. JETP, 14, 393
Norberg P. et al., 2002, MNRAS, 336, 907
Papovich C. et al., 2004, ApJS, 154, 70
Peebles P. J. E., 1993, Principles of Physical Cosmology. Princeton Univ. Press, Princeton, NJ
Pérez-González P. G. et al., 2008, ApJ, 675, 234
Polletta M. et al., 2007, ApJ, 663, 81

Prandini E., Bonnoli G., Maraschi L., Mariotti M., Tavecchio F., 2010, MNRAS, 405, L76

Primack J. R., Bullock J. S., Somerville R. S., MacMinn D., 1999, Astropart. Phys., 11, 93

Primack J. R., Somerville R. S., Bullock J. S., Devriendt J. E. G., 2001, Aharonian F. A., Volk H. H., eds, AIP Conf. Proc. Vol. 558, High-Energy Gamma-Ray Astronomy: International Symposium. Am. Inst. Phys., New York, p. 463

Reddy N. A., Erb D. K., Steidel C. C., Shapley A. E., Adelberger K. L., Pettini M., 2005, ApJ, 633, 748

Reddy N. A., Steidel C. C., Fadda D., Yan L., Pettini M., Shapley A. E., Erb D. K., Adelberger K. L., 2006, ApJ, 644, 792

Rieke G. H., Alonso-Herrero A., Weiner B. J., Pérez-González P. G., Blaylock M., Donley J. L., Marcillac D., 2009, ApJ, 692, 556

Rodighiero G. et al., 2010, A&A, 515, A8

Salim S. et al., 2009, ApJ, 700, 161

Salpeter E. E., 1955, ApJ, 121, 161

Sánchez-Conde M. A., Paneque D., Bloom E., Prada F., Domínguez A., 2009, Phys. Rev. D, 79, 123511

Schawinski K. et al., 2009, MNRAS, 396, 818

Schechter P., 1976, ApJ, 203, 297

Schlegel D. J., Finkbeiner D. P., Davis M., 1998, ApJ, 500, 525

Serjeant S., Harrison D., 2005, MNRAS, 356, 192

Sikora M., Stawarz Ł., Moderski R., Nalewajko K., Madejski G. M., 2009, ApJ, 704, 38

Silva L., Granato G. L., Bressan A., Danese L., 1998, ApJ, 509, 103

Silva L., Maiolino R., Granato G. L., 2004, MNRAS, 355, 973

Skibba R. A. et al., 2009, MNRAS, 399, 966

Soifer B. T., Neugebauer G., 1991, AJ, 101, 354

Somerville R. S., Primack J. R., 1999, MNRAS, 310, 1087

Somerville R. S., Primack J. R., Faber S. M., 2001, MNRAS, 320, 504

Somerville R. S., Hopkins P. F., Cox T. J., Robertson B. E., Hernquist L., 2008, MNRAS, 391, 481

Stecker F. W., Glashow S. L., 2001, Astropart. Phys., 16, 97

Stecker F. W., Malkan M. A., Scully S. T., 2006, ApJ, 648, 774

Stecker F. W., Baring M. G., Summerlin E. J., 2007, ApJ, 667, L29

Strateva I. et al., 2001, AJ, 122, 1861

Takeuchi T. T., Ishii T. T., Dole H., Dennefeld M., Lagache G., Puget J.-L., 2006, A&A, 448, 525

Taylor E. N. et al., 2009, ApJ, 694, 1171

Weekes T. C. et al., 2002, Astropart. Phys., 17, 221

Willmer C. N. A. et al., 2006, ApJ, 647, 853

Wilson J. C. et al., 2003, in Masanori I., Moorwood A. F. M., eds, Proc. SPIE Vol. 4841, Instrument Design and Performance for Optical/Infrared Ground-Based Telescopes. SPIE, Bellingham, p. 451

Wuyts S. et al., 2009, ApJ, 700, 799

Wyder T. K. et al., 2005, ApJ, 619, L15

Xu C. K. et al., 2005, ApJ, 619, L11

Yang J., Wang J., 2010, PASJ, 62, L23

Younger J. D., Hopkins P. F., 2010, preprint (arXiv:1003.4733)

This paper has been typeset from a TEX/LATEX file prepared by the author.